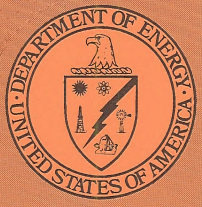

DOE/MC/11577-1384
(DE83009649)

FRACTURE OF DEVONIAN SHALE BY TAILORED PULSE-LOADING

By
S. L. McHugh
W. J. Murri
L. Seaman
D. R. Curran
D. D. Keough

December 1978

Work Performed Under Contract No. AC21-79MC11577

For
Morgantown Energy Technology Center
Morgantown, West Virginia

By
SRI International
Menlo Park, California

TECHNICAL INFORMATION CENTER
UNITED STATES DEPARTMENT OF ENERGY

DISCLAIMER

This report has been reproduced directly from the best available copy.

Available from the National Technical Information Service, U. S. Department of Commerce, Springfield, Virginia 22161.

Price: Printed Copy A05
Microfiche A01

Codes are used for pricing all publications. The code is determined by the number of pages in the publication. Information pertaining to the pricing codes can be found in the current issues of the following publications, which are generally available in most libraries: *Energy Research Abstracts, (ERA); Government Reports Announcements* and Index (*GRA* and I); *Scientific and Technical Abstract Reports (STAR);* and publication, NTIS-PR-360 available from (NTIS) at the above address.

DOE/MC/11577-1384
(DE83009649)
Distribution Category UC-92a

FRACTURE OF DEVONIAN SHALE BY TAILORED PULSE-LOADING

BY

S.L. McHugh, W.J. Murri, L. Seaman,
D.R. Curran, and D.D. Keough
SRI International
333 Ravenswood Avenue
Menlo Park, California 94025

December 1978

Prepared For

United States Department of Energy
Morgantown Energy Technology Center
Morgantown, West Virginia

Under Contract No. DE-AC21-79MC11577

CONTENTS

ILLUSTRATIONS

TABLES

I PROGRAM SUMMARY AND CONCLUSIONS

The Department of Energy (DOE), Morgantown Energy Technology Center (METC) at Morgantown, West Virginia, is examining methods to increase production of natural gas from marginal reserves. Because of the potentially large reserves present in the eastern Devonian shales, these materials have been selected for the application and evaluation of novel and existing well fracturing and stimulation techniques.

As part of this program, SRI International has studied the feasibility of enhancing fracture formation and growth in well stimulation by tailored pulse loading, i.e., shaping the borehole input pressure-time history to produce a specified fracture pattern. Specifically, SRI's computational fracture model, NAG-FRAG, was used to evaluate the effect of pulse shape and rock properties in controlling dynamic rock fracture. Preliminary calculations were made of the amount and location of damage in a cylindrical configuration (Section V), and laboratory-scale springing experiments were performed to determine the NAG-FRAG fracture parameters of the Devonian shale (Section VI).

An exponentially decaying input pressure history was selected as the pulse shape for use in the final pulse shaping calculations (Figure 29b Section VII). It was intended that this pulse shape would provide a simple, smooth, one-parameter description of the pressure history at constant impulse that would be uniquely characterized by the pulse width. However, because calculational instabilities were generated by crack closure and reopening (a difficulty with current fracture codes), it was neccessary to add a constant compressive tail proportional to pulse height. Hence the final pulse shape sensitivities were determined for pulses of various combinations of amplitude and width, but not for constant impulse. This does not affect the general conclusions but does prevent comparison of effects of specific features of the pulse shape. The maximum pulse amplitudes (0.1 to 1.0 GPa) and width of the exponential portion (1 to 10 μs) were selected to be comparable to those used in the experiments. The effect of pulse shape and rock properties on the computed crack densities was then examined by varying the pulse width and NAG-FRAG parameters (Sections VII and VIII).

The results indicate that in general:

- The amount and location of tensile cracking in a cylindrical geometry are strongly dependent on the shape of the pulse applied to the

borehole. The main reason is that the borehole pulse shape strongly affects the circumferential tensile stress which, together with the fracture dynamics, controls rock fracture.

- In the range of stress investigated (up to 1 GPa) the width of the propagated radial stress pulse is determined largely by the geometry and material properties rather than the shape of the borehole pulse.

- The shape of the fracture density distribution for a given pulse shape is not strongly dependent on the values of the NAG-FRAG fracture parameters, but the magnitude of the fracture density is, and therefore it is necessary to determine fracture parameter values for specific shales.

- The magnitude of the circumferential stress occurring in any given annulus of material is little affected by the fracture history of inner annuli; the magnitude is determined more by the impulse than the radial stress.

- Additional calculations are needed in which the interdependence of pulse shape and material properties, such as tensile yield strength, are examined for cylindrical flow.

- A higher density of fractures around the borehole than predicted by radial fracture is probably due to shear cracking, and therefore a shear-cracking model should be incorporated into NAG-FRAG.

- Crack closure and reopening generate instabilities in the calculations. This problem must be solved if the fracture densities for arbitrary pulse shapes are to be evaluated.

II FUTURE WORK

Within the context of the NAG-FRAG model of crack nucleation and growth, results of our feasibility study show that the fracture distribution is stongly dependent on pulse shape, and that quantifying fracture production is strongly dependent on quantifying the NAG-FRAG fracture parameters for each material. However, our laboratory experiments were limited to very small available samples of Devonian shale. The small sample size caused several problems that should be addressed before pulse shaping is considered as a technique for controlling fracture distribution in any well stimulation program. The major problem with the small samples is that the scale of experiments had to be reduced to the point where the borehole size appropriate to the sample diameter limited the variation in pulse width to a narrow range. To have achieved wide variations in pulse widths by adjusting the energy release rates with explosive sources would have required a major effort. In addition, the small diameter resulted in wave reflections, which were minimized but not eliminated by surrounding the samples with a material of matching shock impedance. The small sample also raises questions of the effects of scaling our results to full scale stimulation. For example, do the fracture parameters derived from the laboratory experiments scale?

Because of the importance of enhanced well stimulation, we suggest that efforts be continued to use pulse tailoring to enhance fracture and that field, laboratory, and computational efforts be performed simultaneously. The effects of scaling and pulse shape should be examined computationally for a wider variation in pulse shape, and experimentally in an unbounded sample. The latter would be accomplished by a field effort at a suitable outcrop of shale.

In addition, fracture distributions should be related to rock permeability. Although the present and proposed programs are directed toward enhancing fracture, the ultimate goal is to increase permeability of the *in situ* resource-bearing rock. Establishing desirable fracture distributions requires a thorough knowledge of the permeability of any fracture pattern.

Finally, the present NAG-FRAG model should be completed. Shear fracture is not included, and it is certainly important for describing behavior in the region close to the borehole. In addition, effects of stress relaxation propagation and crack opening and closing should be included. With a more complete model, it would be possible to investigate, computationally, the effect on fracture of more realistic variations in pulse shape parameters.

We suggest that the following three tasks be initiated to accomplish the goals outlined above:

- *Field Effort*--Apply the NAG-FRAG model to larger sample sizes (e.g., using an explosive in a borehole drilled in an outcrop of Devonian shale). This would (a) minimize the problem of stress wave reflection from the sample boundaries encountered in the present program and (b) allow extension of the model to larger flaw sizes to determine the importance of scaling effects (i.e., sample and flaw size) on the predicted crack densities from the NAG-FRAG model.

- *Laboratory Effort*--(a) Accurately determine the fracture parameters of Devonian shale from well sites selected for pulse-tailoring tests, and (b) develop a quantitative method for permeability measurements that will relate the crack size distribution produced in the samples to the permeability.

- *Computational Effort*--Examine the effect of pulse shapes other than an exponentially decaying pulse, and consider the roles that such factors as rise time, decay time and multiple pulses may have in determining the crack density and location in cylindrical geometry. In addition, the model should incorporate shear cracking effects, stress relaxation propagation, and crack closure and reopening. Also, the crack distributions should be related to permeability, to evaluate the role of pulse tailoring in resource recovery.

III INTRODUCTION AND OBJECTIVES

Because of the inherently low permeability of Devonian shale, any stimulation technique applied to it must entail some type of in-formation fracturing. A principal objective of explosive techniques has been to form multiple fractures and/or to propagate preferred fractures by loading the rock dynamically. However, without a detailed knowledge of the relationships between the processes controlling rock fracture and the stress history of dynamic loading, efforts to optimize explosive stimulation are at best trial and error.

Under Contract No. EY-76C-03-0115, SRI International examined the feasibility of enhancing fracture formation and growth in well stimulation by tailored pulse loading. We used the flaw activation and growth concepts of SRI's NAG-FRAG computational subroutine in a one-dimensional wave propagation code, PUFF, to determine the fracture induced in geologic formations by applying dynamic loads.

The three objectives of the program were:

- To determine the relative and absolute importance of various rock properties in controlling rock fracture induced by the dynamic pressure loading of well bores.

- To determine the ranges of the important properties that will permit successful well fracturing by tailored pulse loading, and to correlate these ranges with actual values found in rocks of interest.

- To evaluate the prospects for implementing a well stimulation technique based on pressure-pulse tailoring.

The results of the research performed on pulse tailoring have applications beyond these specific objectives: the fracture models can be directly applied to current or future programs for developing and field demonstrating a propellant-based well stimulation technique; the improved understanding of rock fracture and related processes will prove useful in the study and evaluation of other dynamic stimulation techniques such as the in-formation detonation of high explosives and well bore penetration with shaped charges.

Report Organization--In the following sections, we first describe the NAG-FRAG fracture model (Section IV). The NAG-FRAG model had been developed previously as a computational subroutine. This routine was used with fracture parameters, derived in prior work and representative of shales, to perform preliminary calculations which would guide the laboratory experiments on Devonian shale (Section V). Appendix A describes stress gages used in these experiments. From the laboratory experiments, described in Section VI, we determined the NAG-FRAG parameters characteristic of our shale samples. These parameters were then used in a sensitivity study to determine the effect of parameter variations (Section VII). Finally, we performed a series of calculations in which the pulse shape was varied (Section VIII). From these we determined the sensitivity of fracture to the pulse shape.

IV SRI'S FRACTURE MODEL

SRI research during the past few years has resulted in the development of a computational fracture model based on observed tensile stress-wave-induced activation, growth, and coalescence of inherent flaws in rock and other materials. The model, NAG-FRAG (for crack Nucleation And Growth and FRAGmentation), has shown promising predictive capabilities in studies with Arkansas novaculite and basalt[1,2] and with oil shale.[3,4,5] The input parameters for the NAG-FRAG model include inherent flaw size and orientation distributions, as well as the material properties that govern flaw activation and growth.

In this model, cracks nucleate at inherent flaws and grow until they intersect other cracks or until the stress vanishes. When the cracks intersect, fragments form, and the fragment size distribution can be calculated from the crack size distribution at the time of intersection. If the stress vanishes before the cracks intersect, the material acquires a population of cracks but no fragments. The extent of fracture or the degree of fragmentation resulting from a given loading pulse depends on the number of inherent flaws that are activated by the stress and the rate at which the cracks grow.

The model treats crack densities and orientations in a statistical manner. It does not treat the details of the nucleation, growth, and coalescence of individual cracks, but instead deals with populations of cracks. Therefore, the derived fracture parameters do not describe the behavior of individual cracks, but describe the average behavior of crack arrays. This allows the fracture parameters to be treated as internal state variables in the continuum constitutive relations for the material. The model thus allows the fracturing material to be treated as a continuum with the fracture manifesting itself as a type of work softening.

The NAG-FRAG model was formulated on the basis of observations of fracture in Armco iron, beryllium, novaculite, and Lexan polycarbonate (a transparent plastic).[6] In impact experiments with these materials, fracture occurred by the nucleation and growth of microcracks. These cracks, observed on the sectioned surfaces of the sample, were measured for length and angular orientation with respect to the direction of loading. The observed cracks were organized into groups according to size interval and angle interval. These surface distributions were then transformed statistically to volumetric distributions in size and angle with the BABS2 computer program.[7] For this transformation, it was assumed that the cracks were penny-shaped and that the distribution was axisymmetric around the direction of propagation.

From these experiments, it was determined that the relationship between cumulative crack density and crack size is approximately exponential:

$$N_R = N_o \exp\left[-R/R_1\right] \tag{1}$$

where N_o is the total number of cracks per cubic centimeter, N_R is the number of cracks with radii greater than R, and R_1 is a constant giving the shape of the crack size distribution.

Experiments with Armco iron, polycarbonate, and a quartz phenolic composite, as well as ductile materials in which voids rather than cracks form[6] showed that cracks nucleate at a rate that depends on the tensile stress, σ, normal to the plane of cracks, and that the number of cracks nucleated is governed by the nucleation rate function:

$$\dot{N} = \dot{N}_o \exp\left[\frac{\sigma - \sigma_{no}}{\sigma_1}\right] \tag{2}$$

where $\dot{N}$ is the nucleation rate and $\dot{N}_o$, σ_{no}, and σ_1 are fracture parameters. (Nomenclature for these and other parameters discussed below are given in Table 1, Section V.) $\dot{N}_o$ is the threshold nucleation rate, σ_{no} is the nucleation rate threshold stress, and σ_1 governs sensitivity of nucleation to stress level. Crack growth in this model also depends on the normal tensile stress. The growth law determined from the experiments is

$$\frac{dR}{dt} = \frac{1}{4\eta}(\sigma - \sigma_{go})R \tag{3}$$

where $\frac{1}{4\eta}$ is the growth coefficient,(η describes an effective viscosity of the material at the crack tip), and σ_{go} is the growth threshold stress. The growth threshold stress σ_{go} in metals can be treated as a constant material parameter.

However, in some materials of geologic interest, such as novaculite[8] and oil shale,[3-5] flaw activation is assumed to occur according to Griffith-Irwin fracture mechanics concepts.[8] That is, it is assumed that the applied normal stress will activate flaws larger than a critical radius R^* but leave smaller flaws unaffected. From experiments on these materials, it was found that

Sneddon's relation[9] applies for a penny-shaped crack, subjected to a uniform tensile stress normal to the plane of the crack, in an infinite elastic medium:

$$R^* = \pi \frac{K_{Ic}^2}{\sigma^2} \tag{4}$$

where K_{Ic}, the fracture toughness, is a material property describing the resistance of the material to crack propagation. If σ_{go} is the critical stress for crack growth, then:

$$\sigma_{go} = K_{Ic} \sqrt{\frac{\pi}{R^*}} \tag{5}$$

and hence σ_{go} depends on crack size. The size distribution of inherent flaws is described by two parameters; the nucleation size which is the slope of the size distribution curve and the upper size cutoff which is the maximum inherent flaw size. The size distribution of flaws in the rock sample then governs the number of flaws activated by the normal tensile stress, using Equations (2), (3), and (5).

The main effect of using Equation (5) for σ_{go} instead of using a constant value for this parameter is to skew the calculated crack size distributions toward larger cracks. However, the general results for the two cases are very similar. Since we lacked K_{Ic} values for the Devonian shale, we elected to hold σ_{go} constant in these scoping calculations.

Fragments will form after some amount of crack coalescence, and hence the crack size distribution at fragmentation is assumed to govern the fragment size distribution (using parameters that describe the relationship of cracks to fragments). The process of fragmentation is also modeled in the computational subroutine NAG-FRAG. The NAG-FRAG model contains an algorithm to allow the population of microcracks to increase the compliance of the material and thereby relax the stresses.[10,11]

The fracture-controlling parameters can be determined by performing either uniaxial strain experiments on small specimens (plate impact) or one-dimensional cylindrical experiments in which a charge of high explosive is detonated in a borehole in the material (e.g., a springing experiment). We then quantify the resulting fracture damage and correlate the damage with computed stress histories.[10,11] We used only springing experiments in this project.

To carry out one- and two-dimensional finite-difference calculations for predicting material fracture, it is necessary to know the constitutive relations that control stress wave propagation as well as the fracture parameters. The constitutive relations and material and fracture parameters used in the calculations are discussed in Sections V and VII.

V PRELIMINARY PULSE SHAPING AND FRACTURE PARAMETER SENSITIVITY ANALYSES

A. Preliminary Pulse Shaping Analysis

Because this analysis (and the preliminary fracture parameter sensitivity analysis) was intended to aid the design of the experiments in which the fracture and material parameters would be determined, it was necessary to assume a set of fracture parameters. The fracture properties of Devonian shales are expected to be similar to other shales. Therefore, the initial set of fracture parameters used and the form of the constitutive relations chosen in the preliminary pulse shaping analysis of Devonian shale were derived from previously obtained data[4] on 40 gal/ton oil shale. Calculations were performed in which trial fracture parameters obtained from plate impact data were iterated until reasonable agreement was obtained between the predicted crack size distributions and the crack size distributions previously observed in cylindrical experiments with 40 gal/ton oil shale; the final set of fracture parameters is listed in Table 1.

Although the form of the constitutive relations was that of 40 gal/ton oil shale, the material parameters and the coefficients in the constitutive relations used in the calculations were estimated from Devonian shale data provided by B. Olinger.[12] This allowed more accurate modeling of the distribution of stresses in the Devonian shale produced by explosive loading. The values for the material properties used in the preliminary pulse shaping analysis are given in Table 2.

Olinger[12] determined the bulk and shear moduli directly from ultrasonic measurements. The solid density (ρ_s) chosen for the computations was 2.40 g/cm^3 corresponding to the density measured for the Devonian shale (See Table 3 in Section VI). The remaining parameters were estimated from Olinger's shock and particle velocity data.[12] It was assumed that the hydrostat for the gas shale had the same form as for the oil shale:[3]

$$P = C\mu + D\mu^2 + S\mu^3 \tag{6}$$

where $\mu=(\rho/\rho_s)$ - 1, and C, D, and S were determined to be 3.31×10^{11}, 4.01×10^{11}, and 1.10×10^{12} dyn/cm^2, respectively.

Table 1

FRACTURE PARAMETERS USED IN
PRELIMINARY ANALYSES FOR DEVONIAN SHALE
(Calculation Designation: GS-4*)

Parameter	Numerical Values	Dimensions
Growth coefficient, $\frac{1}{4\eta}$, T_1	-0.02	$cm^2/dyn\text{-}sec$
Growth threshold stress, σ_{go}, T_2	-5.00×10^6	dyn/cm^2
Nucleation size parameter, R_1, T_3	4.00×10^{-3}	cm
Nucleation rate coefficient N_o, T_4	2.00×10^6	$\frac{number}{cm^3\text{-}sec}$
Nucleation threshold stress, σ_{no}, T_5	-1.00×10^8	cyn/cm^2
Stress sensitivity factor, σ_1, T_6	-7.50×10^7	dyn/cm^2
Upper size cutoff for nucleation, T_7	10.00	cm
Threshold stress for entering subroutine, T_8	-1.00×10^8	dyn/cm^2
Ratio of number of fragments to number of cracks, T_{10}	0.33	--
Ratio of fragment radius to crack radius, T_{11}	1.00	--
ΣNR^3 at coalescence, T_{12}	0.20	--
Coefficient for calculating fragment volume, T_{13}	0.30	--

*The following additional calculations were performed with individual fracture parameters set at the indicated value and the remaining parameter values identical to calculaiton GS-4:

GS-5: $T_1 = -2.00 \times 10_5^{-3}$ $cm^2/dyn\text{-}sec$
GS-7: $T_4 = 2.00 \times 10_5^{7}$ $no./cm^3\text{-}sec$
GS-8: $T_4 = 2.00 \times 10^7$ $no./cm^3\text{-}sec.$

Table 2

MATERIAL PROPERTIES USED IN
PRELIMINARY ANALYSES FOR DEVONIAN SHALE

C	Bulk modulus*	3.31×10^{11} dyn/cm^2
D	Quadratic modulus*	4.01×10^{11} dyn/cm^2
S	Tertiary modulus*	1.10×10^{12} dyn/cm^2
Y	Yield strength†	1.16×10^{9} dyn/cm^2
G	Shear modulus	1.57×10^{11} dyn/cm^2
ρ_s	Solid density	2.40 g/cm^3

*Used to define the hydrostat: $P = C\mu + D\mu^2 + S\mu^3$ where $\mu = \frac{\rho}{\rho_s} - 1$ and P is the pressure.

†A von Mises yield criterion was used to model the response of the shale to dynamic loading.

In this analysis, the NAG-FRAG model was incorporated into a one-dimensional stress wave propagation code, PUFF.[13] The computations were performed for a cylindrical geometry and a 500-psi confining pressure in order to model field experiments on Devonian shale as well as to compare the preliminary predicted crack size distributions with similar experiments previously performed on oil shale. Figure 1(a) shows the positions and dimensions of the borehole (filled with PETN at a density of 0.60 g/cm^3 and producing a CJ pressure of 33 kbar) and zones from one 40 gal/ton oil shale laboratory experiment. Figure 1(b) shows the layout used in the calculations to model the experiment and to predict the crack density distributions for variations in the parmeters.

In the calculations for Devonian shale a crack size density distribution was determined for each cell. To facilitate comparison between observations and predictions, the predicted crack size distributions in Devonian shale were taken from cells corresponding to the midpoint of each zone in the oil shale experiment (Figure 1(b)).

To compare the expected effects produced in the crack density distributions in Devonian shale by variations in the material and fracture properties, we examined the effects of variations in the pulse shape of the input pressure to the Devonian shale. In our initial attempts to quantify the effects of variations in the input pressure history on the crack size distribution, we used the material properties listed in Table 2 and the fracture parameters listed in Table 1 (GS-4). However, the pulse shape was varied by changing the Grüneisen ratio γ in the PETN equation of state[14,15] from 0.10 to 3.00. Figure 2 shows the effect of variations in γ on the stress histories, and Figure 3 shows the effect on the radial crack size distribution.

Although varying γ produced large variations in the amplitude and duration of the input pressure, the radial crack size distributions were nearly identical. Close comparison of the predicted stresses in the zones shows that the zones may have experienced very similar circumferential tensile stress histories in spite of the large variations in input pressure; this is probably because both the amplitude and duration of the input pressure were varied simultaneously by changes in γ. For example, increasing γ decreased the duration of the compressive pulse, but increased its amplitude. The individual crack size distribution depends strongly on the tensile stress history experienced by individual zones. Hence, to determine the dependence of the crack size distribution on the input pressure history, it is necessary to consider in more detail the relationship between the tensile stress history in the zones and the input pressure history.

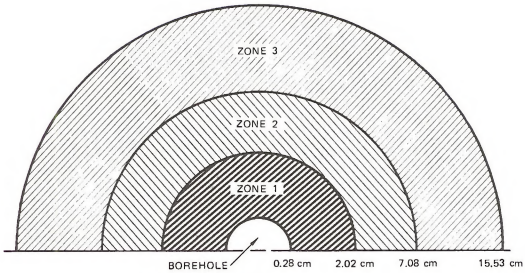

(a) POSITION AND DIMENSIONS OF ZONES

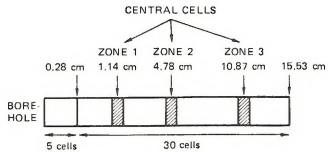

(b) POSITIONS OF CELLS

Cell positions corresponding to midpoints of zones 1, 2, and 3 are crosshatched.

MA-6700-8

FIGURE 1 CONFIGURATION USED IN ONE-DIMENSIONAL CYLINDRICAL GEOMETRY CALCULATIONS TO PREDICT CRACK SIZE DISTRIBUTIONS

From 40 gal/ton oil shale experiment.

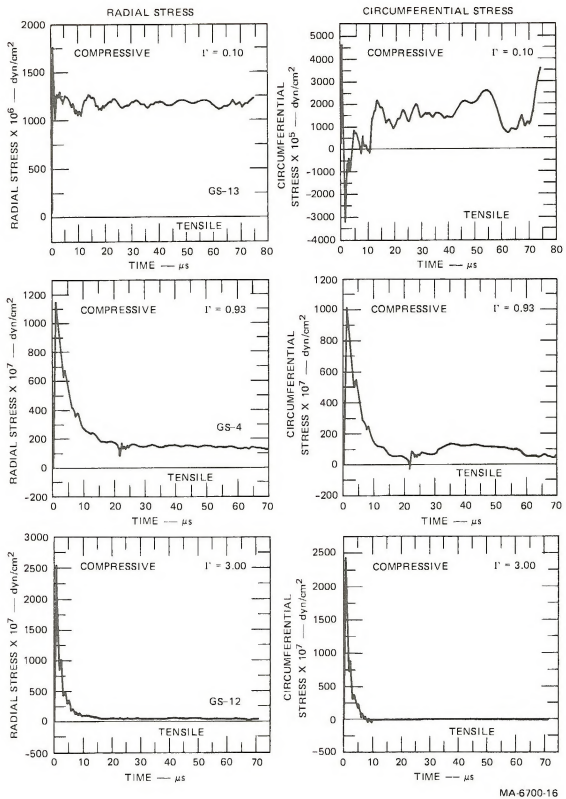

FIGURE 2 RADIAL AND CIRCUMFERENTIAL "DAMAGE" STRESSES PREDICTED AT BOREHOLE-SHALE BOUNDARY FOR VARIATIONS IN EXPLOSIVE (PETN) EQUATION OF STATE

Computed using fracture parameters in Table 1, GS-4.

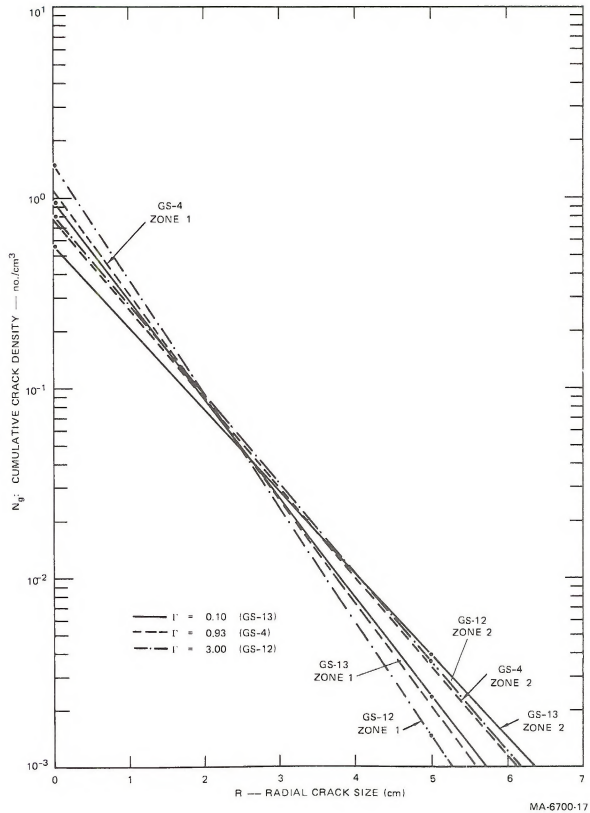

FIGURE 3 PREDICTED RADIAL CRACK SIZE DISTRIBUTION IN ZONES 1 AND 2 ASSOCIATED WITH CIRCUMFERENTIAL "DAMAGE" STRESSES IN FIGURE 2

Two additional calculations were performed to (1) qualitatively evaluate the effect of pulse shape on the radial crack size density distributions and (2) explore in more detail the relationship of the tensile stresses in individual zones to the input compressive stress history. The material and fracture parameters used in these calculations were again those in Tables 1 and 2. The one-dimensional cylindrical geometry used is shown in Figure 4; it differs slightly from that in Figure 1 to accommodate specification of an arbitrary pressure history at the borehole perimeter.

In one calculation, labeled GS-21, the peak pressure is higher and the duration longer than in the other labeled GS-23. In the case of GS-21, an explosive was assumed to fill the borehole to simulate a constant volume explosion. In the case of GS-23, the pressure history, P(t), was specified at the borehole boundary as

$$P(t) = e^{-\left[t/t_0\right]^2} \tag{7}$$

where t_0 is one microsecond. Figure 5 shows the resulting radial and circumferential stress histories (positive in compression, negative in tension) and the associated damage histories. The damage parameter is the effective radial crack area (defined as the product of the total radial crack density, N_0, and the square of the characteristic radial crack size, R_1, that is, $A = N_0 R_1^2$). Figure 6 shows the radial crack density distributions (before the stress wave reflects from the outer boundary) for these two cases.

The maximum shock velocity at the peak stress of these calculations in this material is 4.77 mm/μs, and consequently, the outer boundary does not influence the stress or damage histories within the first 50 to 60 μs. Therefore, these crack density distributions are equivalent to those expected in an infinite medium--in which damage is caused by the outgoing stress wave.

Although in GS-21 the input peak radial compressive stress, σ_r, and the input peak circumferential compressive stress, σ_θ (Figure 5 at d = 0.30 cm), are larger by about a factor of two than those in GS-23, σ_θ in GS-23 becomes tensile and produces damage much earlier than in GS-21. More damage is predicted near the borehole in GS-23, and far from the borehole in GS-21, because the tensile stresses are large in these regions (Figure 6).

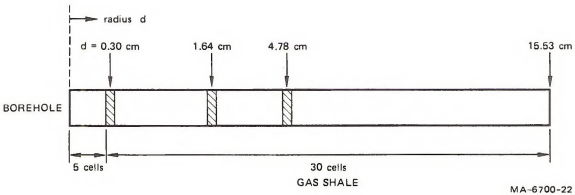

FIGURE 4 CONFIGURATION USED IN ONE-DIMENSIONAL CYLINDRICAL GEOMETRY CALCULATIONS TO PREDICT CRACK SIZE DISTRIBUTIONS IN GAS SHALE

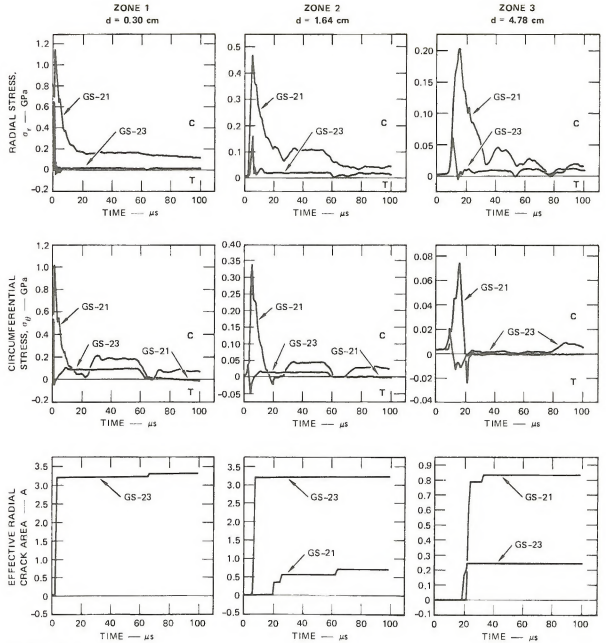

C = Compression

T = Tension

d = radial distance from center of borehole

MA-6700-23

FIGURE 5 COMPARISON OF STRESS AND DAMAGE HISTORIES PRODUCED BY TWO DIFFERENT PULSE SHAPES

Calculated using PUFF and NAG-FRAG, with cell positions shown in Figure 4.

GS-21: Input pressure computed using PETN equation of state.

GS-23: Input pressure specified as $P(t) = 1.0\ \text{GPa}\ e^{-(t/10^{-6}_{s})^2}$

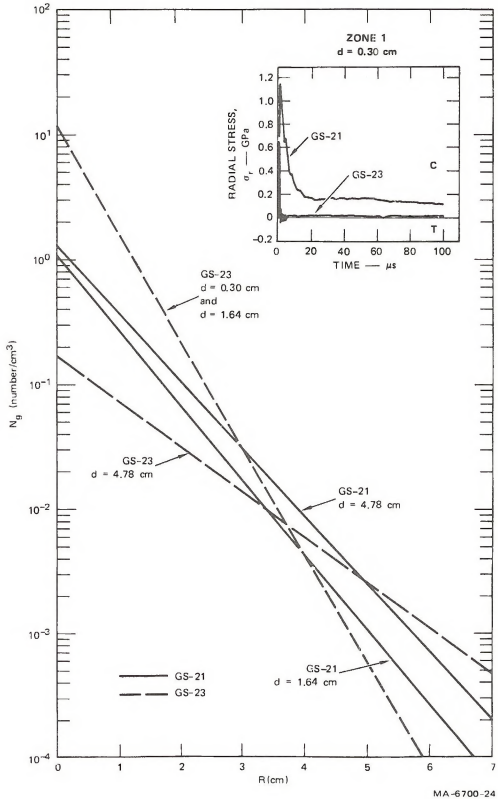

FIGURE 6 PREDICTED RADIAL CRACK SIZE DISTRIBUTIONS FOR THE CELL POSITIONS SHOWN IN FIGURE 4 AND ASSOCIATED WITH THE CIRCUMFERENTIAL STRESS HISTORIES SHOWN IN FIGURE 5

Thus, a low amplitude and short duration input compressive pulse, which decays rapidly to zero pressure, would produce a steep tensile damage gradient (damage decreases rapidly away from the borehole), whereas a high amplitude and large duration input compressive pulse would cause little tensile cracking close to the borehole, and more tensile cracking far from it.

These examples illustrate that variations of pressure history at the borehole boundary may significantly affect the fracture distribution in a fairly straightforward manner. However, because the impulse is not constant in these cases, it was expected that the fracture distributions would differ.

B. Preliminary Fracture Parameter Sensitivity Analysis

The preliminary fracture parameter sensitivity analysis was also intended to guide the design of the later springing experiments. Consequently, as with the preliminary pulse shaping analysis, a set of material and fracture parameters had to be assumed in order to perform the computations. The parameters used in this preliminary analysis are those used in the preliminary pulse shaping computations and are listed in Tables 1 and 2. (Calculations GS-4, GS-5, GS-7, and GS-8 are summarized in Table 1.)

The positions and dimensions of the borehole and zones (Figure 1), as well as the PETN model, are those used in the preliminary pulse shaping analysis. As before, the predicted crack size distributions in the Devonian shale were taken from computational cells corresponding to the midpoint of each zone in the oil shale to facilitate comparison between observations of crack densities in the oil shale and predictions of crack densities in the gas shale [Figure 1(b)].

The predicted "no damage" radial and circumferential stresses for zones 1 and 2 are shown in Figure 7. ("No damage" corresponds to infinite tensile strength: fracturing is not allowed to occur.) Compressive stresses are positive and tensile stresses are negative. The effect of fracture on the stress histories is shown in Figure 8. The compressive stresses are not significantly altered but the tensile stresses are greatly modified, as seen in Figure 9, because of the increased tensile compliance and eventual failure caused by crack growth.

Previous work on 40 gal/ton oil shale[5] has shown that the crack density distributions predicted by the NAG-FRAG computational subroutine are significantly affected by variations in the fracture parameters T_1 (the growth coefficient $\frac{1}{4\eta}$, from Equation 3, Section IV) and T_4

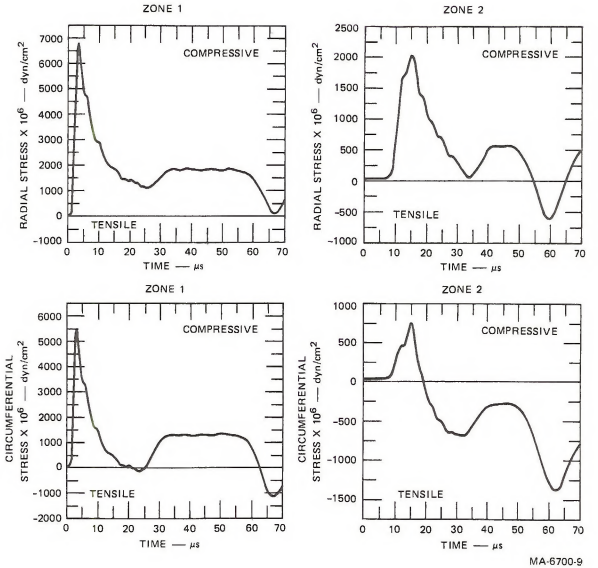

FIGURE 7 PREDICTED "NO DAMAGE" RADIAL AND CIRCUMFERENTIAL STRESS HISTORIES IN ZONES 1 AND 2 IN DEVONIAN SHALE

Material properties from Table 2.

Zone positions from Figure 1 (b).

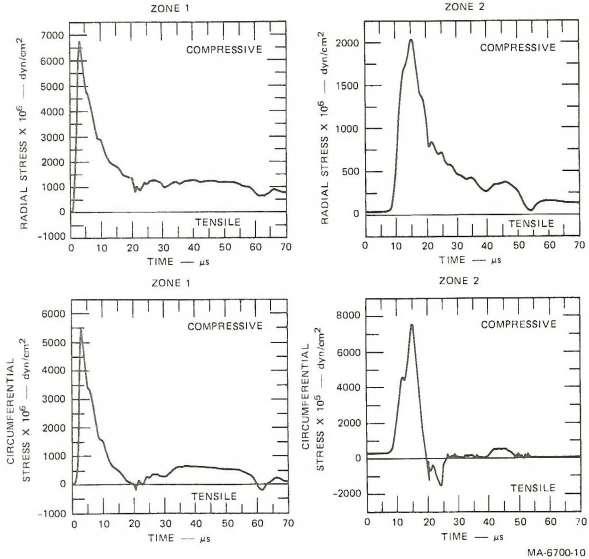

FIGURE 8 PREDICTED "DAMAGE" RADIAL AND CIRCUMFERENTIAL STRESS HISTORIES IN ZONES 1 AND 2 FOR DEVONIAN SHALE

Preliminary fracture parameters from Table 1 (GS-4) and material properties from Table 2.

Zone positions from Figure 1 (b).

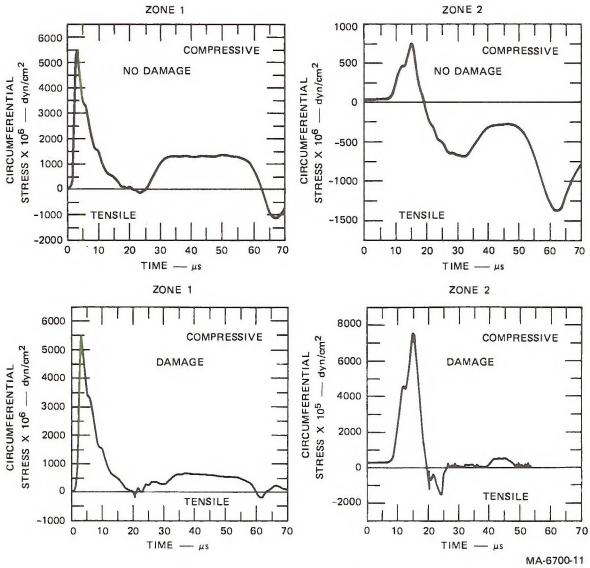

FIGURE 9 PREDICTED "NO DAMAGE" AND "DAMAGE" CIRCUMFERENTIAL STRESS IN ZONES 1 AND 2 FOR DEVONIAN SHALE (FROM FIGURES 7 AND 8)

"Damage" stress computed using fracture parameters in Table 1, GS-4.

Zone positions from Figure 1 (b).

($\dot{N}_o$, the total nucleation rate from Equation 2). Therefore, we expected the crack density distribution in Devonian shale to be affected by variations in these parameters also.

The stress histories and radial crack size distributions for two variations of fracture parameters T_1 and T_4 are shown in Figures 10 through 13. Figure 10 shows the stress history resulting when T_1 is varied from -2.00×10^{-2} to -2.00×10^{-3} $cm^2 dyn^{-1} sec^{-1}$. In Figure 11, the stresses predicted using a nucleation rate (T_4 or $\dot{N}_o$) of 2.00×10^6 $no.\ cm^3\ sec^{-1}$ (T_4 from Table 1, GS-4) are compared with the stresses predicted using a nucleation rate of 2.00×10^7 $no.\ cm^{-3}\ sec^{-1}$ (T_4 from Table 1, GS-8). Although variations in T_1 and T_4 affect the crack size distributions by orders of magnitude, e.g., curves GS-4, zone 2 and GS-5, zone 2 of Figure 12, the effects on the stress histories are moderate (change of five in stress and two in duration) for the variation of T_1 (Figure 10) and almost negligible for the variation in T_4 (Figure 11).

Figure 13 summarizes the effects of variations in $\dot{N}_o$ on the radial crack size distributions;

$$2.00 \times 10^5 no.cm^{-3}sec^{-1} \leqslant \dot{N}_o \leqslant 2.00 \times 10^7\ no.\ cm^{-3}\ sec^{-1}.$$

In this range, the logarithms of the total radial crack density and the slope of the distribution, R_1, vary linearly with the logarithm of the nucleation rate.

The preliminary results demonstrated that the crack density distributions produced by explosive loading in Devonian shale will be sensitive to the material and fracture properties, given by T_1 and T_4. Therefore, these properties must be adequately characterized (as described in Section VI) prior to performing both the final fracture parameter sensitivity analysis (Section VII) and final pulse shaping analysis (Section VIII). The results of the preliminary parameter sensitivity analysis illustrated that large changes in the fracture parameter, $\dot{N}_o$, will produce similar large changes in the total crack density, N_o, and smaller changes in the characteristic crack size, R_1.

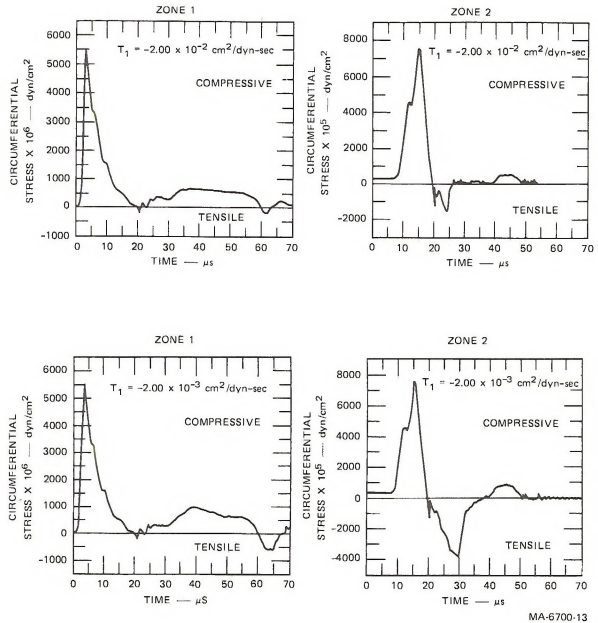

FIGURE 10 PREDICTED CIRCUMFERENTIAL STRESS HISTORIES IN ZONES 1 AND 2 FOR TWO "DAMAGE" CASES (GS-4 and GS-5) IN DEVONIAN SHALE

Fracture parameter T_1 (the growth coefficient, $1/4\eta$) decreases from -2.00 x 10^{-2} cm^2/dyn-sec to -2.00 x 10^{-3} cm^2/dyn-sec; and T_4 = 2.00 x 10^{-6} no./cm^3-sec (all other parameters held constant).

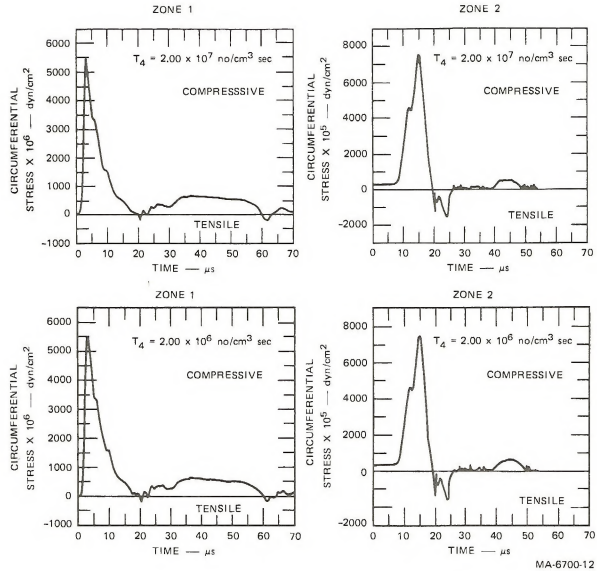

FIGURE 11 PREDICTED CIRCUMFERENTIAL STRESS HISTORIES IN ZONES 1 AND 2 FOR TWO "DAMAGE" CASES (GS-4 AND GS-8) IN DEVONIAN SHALE

Fracture parameter T_4 (the nucleation rate $\dot{N}_o$) was increased from 2.00 x 10^6 no/cm^3-sec to 2.00 x 10^7 no/cm^3-sec, and T_1 = 2.00 x 10^{-2} cm^2/dyn-sec.

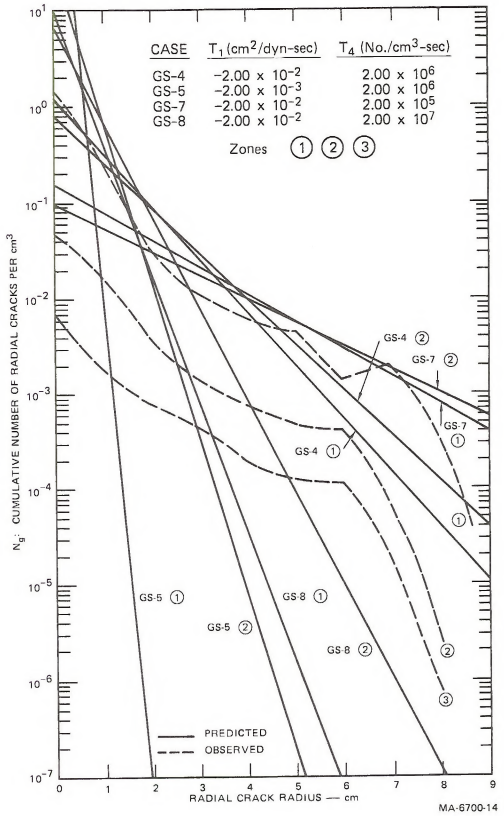

FIGURE 12 EFFECT ON PREDICTED RADIAL CRACK SIZE DISTRIBUTION FOR DEVONIAN SHALE OF VARIATIONS IN SELECTED PRELIMINARY FRACTURE PARAMETERS FOR ZONES 1 AND 2 (Table 1)

Observed radial crack size distribution in zones 1, 2, and 3 from 40 gal/ton oil shale experiment (Figure 1 (a)) shown for comparison.

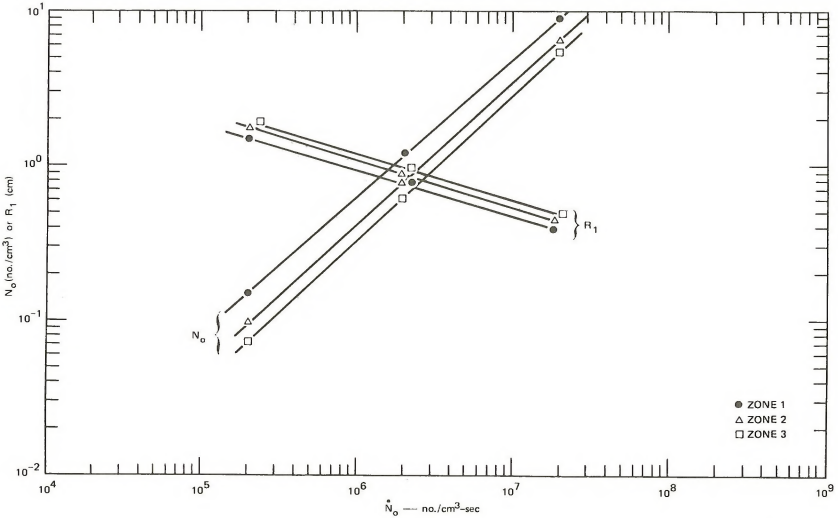

MA-6700-15

FIGURE 13 PREDICTED DEPENDENCE OF TOTAL RADIAL CRACK DENSITY (N_0) AND CHARACTERISTIC CRACK SIZE (R_1) ON NUCLEATION RATE ($T_4 = \dot{N}_0$) IN ZONES 1, 2 AND 3 — Summarized from Figure 12.

VI MATERIAL CHARACTERIZATION

The preliminary parameter sensitivity analysis indicated that the predictions of crack density from the NAG-FRAG model are fairly sensitive to at least some of the material properties, and the preliminary pulse shaping analysis indicated that the effect of pulse shape on the crack density distribution is also significant. These results implied that before calculating the effect of shaping the input pressure history on the crack density distribution, it was necessary to know the material and fracture properties of Devonian shale and the variations in those properties.

Therefore, cores of Devonian shale were acquired and measurements of the bulk material properties were made. Because of the importance of the microstructure to fracture, observations were made of inherent flaws and cracks produced by explosive loading. Springing experiments were performed to determine the fracture parameters of Devonian shale in the NAG-FRAG model.

A. Sample Acquisition and Initial Preparation

We obtained six cores (10.2 cm in diameter and up to 51 cm long) of Devonian shale from Dr. Paul Dumontelle of the Illinois State Geological Survey (ISGS). These cores were used in all the material property tests and experiments. A segment 30.5 cm in length was removed from the center portion of each of four shale cores and was jacketed with a layer of Castall 300* Epoxy (approximately 1 cm thick). The epoxy served several purposes. During storage and handling, it prevented water loss and mechanical abrasion. In laboratory experiments, it prevented intrusion of the surrounding fluid used to provide confining pressure; it also increased the effective diameter of our samples, since they were only marginally sufficient for the scale of the experiment. To be effective, the shock impedance of the epoxy must be matched to that of the shale. If properly matched, waves reflected from the periphery of the jacketed sample will not affect the fracture distribution in the shale.

*Obtained from Castall Inc., Weymouth Industrial Park, East Weymouth, MA 02189

B. Microstructure

1. Inherent Flaws

Observations of the initial microstructure of the shale are important because the formation and propagation of cracks in the shale during explosive loading depend on its microstructure and because preexisting or inherent flaws may bias the determination of a crack size distribution after explosive loading.

Two samples of Devonian shale with surface areas of about $1 cm^2$ were prepared for observation in the scanning electron microscope (SEM). The samples were taken from sections corresponding to the 584- and 587-foot depth intervals of the original core. They were cut from the end pieces remaining after the 30.5 cm sections were removed from the cores, mounted in epoxy, and lapped with 0.3 μm diamond paste. The epoxy jacket was then removed to facilitate loading into the SEM, and a 200 Å layer of gold-palladium was sputtered onto the surface to prevent charge accumulation during SEM viewing.

Figures 14 and 15 are scanning electron photomicrographs of the samples. In general, they appear to be relatively homogeneous with no apparent microstructural features, such as layering or micrometer- to millimeter-sized fractures. Sample 2, shown in Figure 15, appears denser than Sample 1 in Figure 14. One small fracture was observed in Sample 2 (Figure 15), although the flaw may be, instead, a slight separation between adjacent grains.

Though we examined the microstructure of these samples to gain insight into the physical mechanism responsible for the formation and growth of cracks during later experiments, we were also able to qualitatively determine the distribution of elements in the samples from the x-ray scans. Some Ca and Mg was observed in the euhedral grains, and large amounts of Si were seen in the other grains. Some Fe and S were also detected. Although no hydrocarbon was directly detected during the scans, the relative lack of elements heavier than oxygen observed in the x-ray scans between the grains suggests that hydrocarbon is present in the rubblelike material.

These observations suggest that individual grains may be chemically distinct and poorly bonded and that fracture will occur by separation along grain boundaries. After the dynamic

1 cm = 100 μm

(a) 100 MAGNIFICATION
Si PREDOMINATES IN THIS REGION, BUT Ca AND Mg WITH TRACES OF Fe AND S WERE OBSERVED IN X-RAY SCANS.

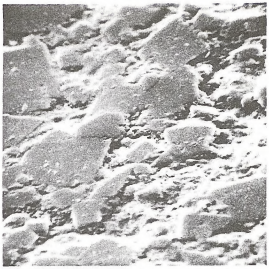

1 cm = 20 μm

(b) 500 MAGNIFICATION
SAME Ca AND Mg WAS OBSERVED IN X-RAY SCANS OF THE EUHEDRAL GRAINS.

1 cm = 2 μm

(c) 5000 MAGNIFICATION

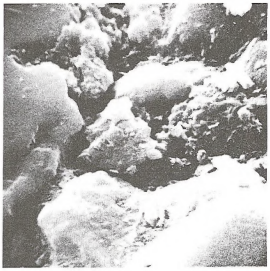

1 cm = 2 μm

(d) 5000 MAGNIFICATION
THE PRESENCE OF HYDROCARBON IN THE RUBBLE LIKE MATERIAL (BETWEEN GRAINS) WAS INFERRED FROM X-RAY SCANS.

MP-6700-4

FIGURE 14 SCANNING ELECTRON PHOTOMICROGRAPHS OF DEVONIAN SHALE: SAMPLE 1 FROM 584-FOOT DEPTH INTERVAL

1 cm = 20 μm

(a) 500 MAGNIFICATION
NOTE THAT INDIVIDUAL GRAINS ARE INDISTINCT AND THE MATERIAL APPEARS DENSER THAN THAT IN SAMPLE 1. THE FLAW SHOWN IN (b) AND (c) CAN BE SEEN IN THE UPPER MIDDLE OF THIS PHOTOGRAPH.

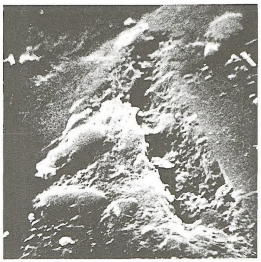

1 cm = 2 μm

(b) 5000 MAGNIFICATION
ONLY THIS FLAW WAS OBSERVED IN THE SAMPLE.

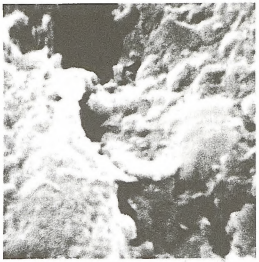

1 cm = 0.5 μm

(c) 20,000 MAGNIFICATION
CLOSE-UP OF THE FLAW SHOWN IN (b).

MP-6700-5

FIGURE 15 SCANNING ELECTRON PHOTOMICROGRAPHS OF DEVONIAN SHALE: SAMPLE 2 FROM 587-FOOT DEPTH INTERVAL

loading experiments were completed, samples were taken from the cores and their microstructures were examined to determine if fracturing had indeed occurred by separation along the grain boundaries, as discussed below.

2. Explosively Induced Cracks

Two samples (surface areas of 1 cm^2) of Devonian shale were prepared for the SEM after the two springing experiments were completed. The cylinders were sectioned and photographed, and then samples were cut from around the borehole. As before, the samples were mounted in epoxy and lapped with 0.3-μm diamond paste. The epoxy jacket was removed to facilitate loading into the SEM, and a 250 Å layer of silver was sputtered onto the surface to prevent charge accumulation during SEM viewing.

Figures 16 and 17 are the scanning electron photomicrographs of these samples. The circumferential crack, around the borehole, was probably caused by shrinkage of the epoxy during sample preparation. The radial cracks, however, were probably present before sample preparation and may have been caused by the explosive.

The cracks appear to be caused by separation along grain boundaries, as expected. Figures 17(b) and 17(c) show branching of one of the cracks. However, there is not a continuous distribution of radial crack sizes, nor is there extensive cracking around the borehole. Such low crack densities might indicate that minor compaction, rather than cracking, occurred around the borehole.

C. Bulk Material Property Determination

The determination of the bulk material properties is important because some of these parameters (e.g., density, bulk modulus, and shear modulus) are used as inputs to the stress-wave propagation and fracture distribution computations.

To determine density, sound velocity, and moisture content, we took samples from both ends of each core section, hoping that these measurements would bracket the variation through the core. The density was determined by water displacement. Sound velocity was measured perpendicular to the bedding on all specimens. In addition, three specimens were measured parallel to the bedding. The measured values are given in Table 3. Moisture content was

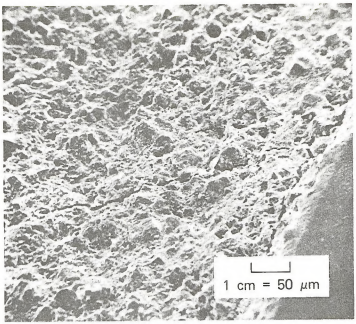

(a) EXPLOSIVELY INDUCED RADIAL CRACK IN DEVONIAN SHALE
Borehole is at right.

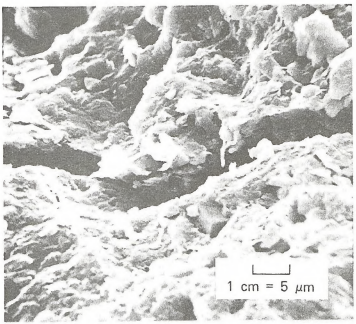

(b) CLOSE-UP OF EXPLOSIVELY INDUCED RADIAL CRACK

MP-6700-31

FIGURE 16 CRACK PRODUCED IN SPRINGING EXPERIMENT GSC-1 (SEM)

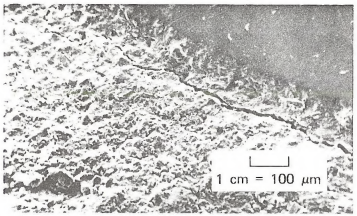

(a) BOREHOLE AT UPPER RIGHT, CIRCUMFERENTIAL CRACK PROBABLY PRODUCED DURING SAMPLE PREPARATION

Other cracks probably produced by explosive.

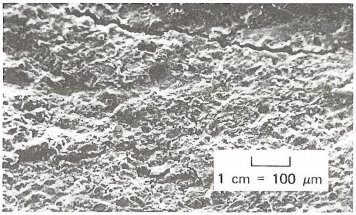

(b) CIRCUMFERENTIAL CRACK AROUND BOREHOLE, AT TOP

Note branching of crack in center of photograph.

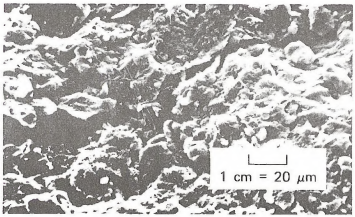

(c) DETAIL OF CRACK BRANCHING FROM (b).

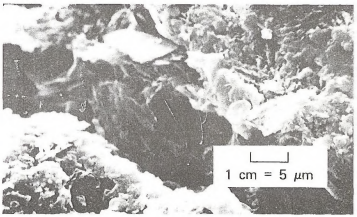

(d) DETAIL OF CRACK IN (b).

MP-6700-32

FIGURE 17 CRACK PRODUCED IN SPRINGING EXPERIMENT GSC-2 (SEM)

Table 3

MATERIAL PROPERTIES OF DEVONIAN GAS SHALE

Core Depth (ft)	Density (g/cm^3)	Moisture Content (wt%)	Sound Velocity	
			Perpendicular to Bedding (mm/μsec)	Parallel to Bedding (mm/μsec)
496	2.44	2.4	2.59	3.88
497	2.45	2.0	2.37	
565	2.44	1.8	2.37	
566	2.50	5.5	2.62	3.48
586	2.53	3.6	3.24	4.21
587	2.43	6.3	3.27	
588	2.46	5.8	3.40	

determined from the weight loss after specimens were heated in an oven for 36 hours at 110°C. These data are also given in Table 3.

From the variations found in bulk material properties, it may be expected that the fracture properties of the Devonian shale are also variable. Consequently, an analysis of the effect of pulse shaping must also examine effects produced by variable material properties (Sections VII and VIII).

D. Derivation of Material and Fracture Properties of Devonian Shale

Springing (i.e., small-scale, cylindrical) experiments were made to determine the material and fracture properties of the Devonian shale for use in the parameter sensitivity analyses and pulse shaping (Sections VII and VIII).

1. Design of Experiments

Two 10.2 cm diameter cores provided by the ISGS were selected, and a 7.5 mm diameter borehole was drilled along the axis. Figures 18 and 19 show a diagram and a photograph, respectively, of the configuration. One core, for experiment GSC-1, was sectioned parallel to the axis at 9 mm and 30.2 mm from the edge of the borehole. Ytterbium stress gages (A-1, A-2, A-3, B-1 in Figure 18) were emplaced, and the sections were epoxied together. The other core (experiment GSC-2) did not contain any gages in the shale. Two T-shaped (1 mm x 5 mm) ytterbium stress gages (Ex 1, Ex 2 in Figure 18) were emplaced in each borehole to monitor the stress history at the borehole-shale interface. Experiments testing these gages are described in the Appendix. During the experiments, the cores were epoxied (using Castall 300) into a 30.5-cm-O.D. aluminum jacket to ensure that the radial stress reflection from the shale periphery was compressive, thereby minimizing tensile cracking in the circumferential direction. An ytterbium stress gage (C1 in Figure 18) was placed at the epoxy-aluminum interface in both experiments.

The explosive source in both experiments was 1.8 mm (0.070 in.) diameter MDF (5 grains PETN/foot, 1.3 g/cm^3). In experiment GSC-1, the MDF was surrounded by a 7.5 mm O.D. lucite sleeve. In experiment GSC-2, the MDF was surrounded by a 7.5 mm O.D. air gap. Preliminary calculations indicated that the input pressure to the shale in GSC-1 (using the lucite sleeve) would be four to five times larger than in GSC-2 (using the air gap) and that

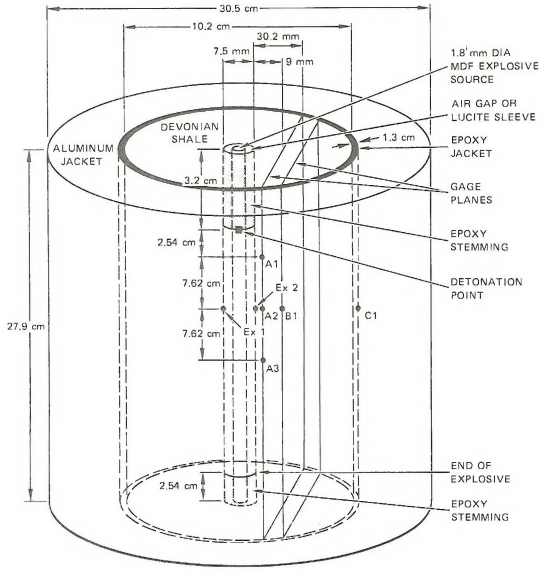

FIGURE 18 CONFIGURATION OF SPRINGING EXPERIMENTS

Gage planes in Devonian shale present for experiment GSC-1, but not for GSC-2.

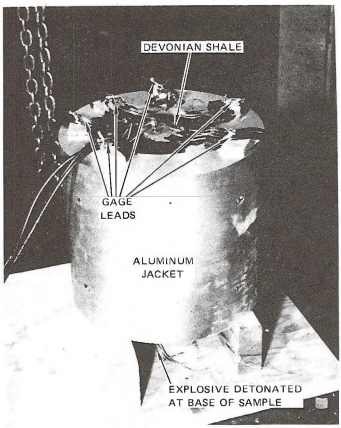

FIGURE 19 PHOTOGRAPH OF SPRINGING EXPERIMENT SHOWING DEVONIAN SHALE CORE WITH ALUMINUM JACKET AND ELECTRICAL CONNECTIONS

their pulse widths (2 to 3 μs) would be comparable. Thus, the experiments would test the effect of pulse shape on the crack distributions.

2. Results

The MDF was detonated using an exploding bridgewire detonator. The voltage-time histories from the gages were recorded on oscilloscopes and are shown in Figure 20. These data were digitized and corrected for the gage response; they are shown as compressive stress histories in Figure 21. The peak compressive stress and pulse duration recorded by each gage are given in Table 4.

After detonation of the MDF, the aluminum jacket was removed from the Devonian shale core, and the core was sectioned at the midlength position perpendicular to the axis. The shale sections were ground and polished in kerosene, and lapped with 0.3 μm aluminum oxide powder.

The crack patterns from the two experiments are shown in Figures 22 and 23. The peak radial compressive stresses (Table 4) recorded by the borehole gages in GSC-1 and GSC-2 were 0.36 to 0.45 GPa and 0.40 to 0.50 GPa, respectively. Although preliminary calculations indicated that the peak radial compressive stress in GSC-1 should be greater than that in GSC-2 by a factor of four to five, in GSC-1 the stress was slightly less than that in GSC-2. The reason for this discrepancy appears to be that the borehole vented at detonation in GSC-1, thereby reducing the pressure.

The crack patterns (Figures 22 and 23) are fairly similar. The cracking (with the exception of the cracks disturbed by the gage planes) is essentially radial, with cracks extending from the borehole to the shale boundary. The azimuthal distribution of cracks is not uniform; rather there is approximately a 120 degree separation between the cracks. A few small cracks are present around the borehole.

The crack density distribution was compared to the distribution predicted by NAG-FRAG. This was done by counting and converting to a volume distribution the number of cracks of a given length and orientation per square centimeter exposed on these sections. First, the crack size distribution was determined for each section by splitting each section into three concentric zones centered on the borehole, then determining the length and orientation of each crack in each zone, and then counting the number of cracks within a specified length and orientation

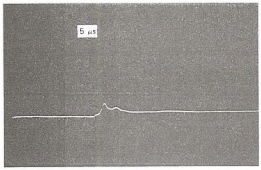

Ex 1

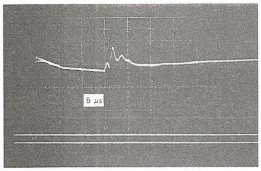

Ex 2

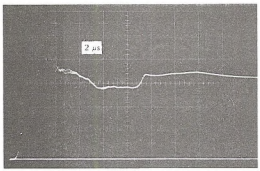

A1

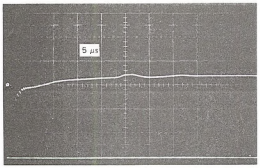

A2

(a) GSC-1

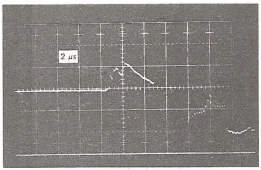

Ex 1

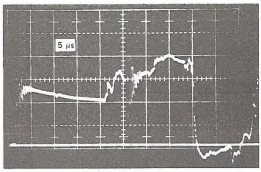

Ex 2

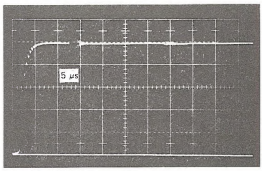

C1

(b) GSC-2

MP-6700-27

FIGURE 20 VOLTAGE RECORDS FROM SPRINGING EXPERIMENTS

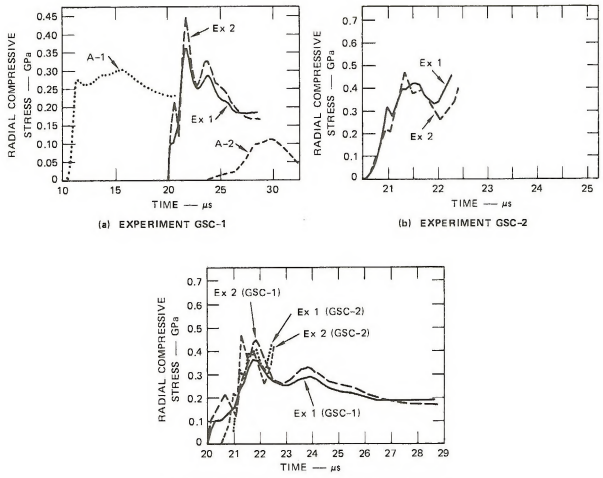

FIGURE 21 RADIAL COMPRESSIVE STRESS HISTORIES IN SPRINGING EXPERIMENTS

Explosives detonated at time zero.

Table 4

PEAK RADIAL COMPRESSIVE STRESS AND PULSE DURATION RECORDED FROM SPRINGING EXPERIMENTS

Experiment GSC-1 (7.5 mm O.D. lucite sleeve around 1.8 mm lead-sheathed MDF)			Experiment GSC-2 (7.5 mm O.D. air gap around 1.8 mm lead-sheathed MDF)		
Gage	Stress (GPa)	Duration (μs)	Gage	Stress (GPa)	Duration (μs)
Ex 1	0.36	2 to 3	Ex 1	0.42	1
Ex 2	0.45	2 to 3	Ex 2	0.48	1
A1	0.32	> 5	None		
A2	0.11	6	None		
A3	No data		None		
B1	No data		None		
C1	No data		None	$<2.0 \times 10^{-2}$	Not determined

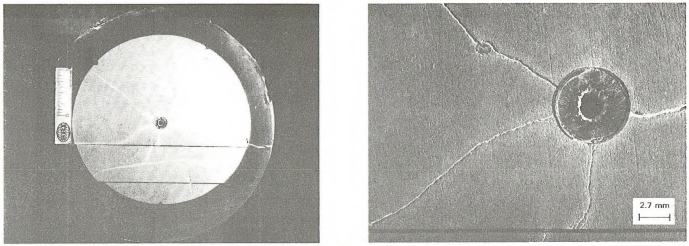

(a) EXPERIMENT GSC-1: LUCITE SLEEVE AROUND MDF EXPLOSIVE SOURCE

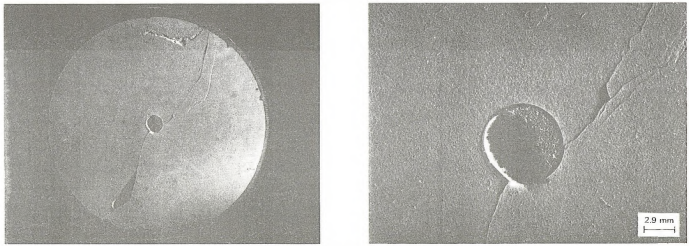

(b) EXPERIMENT GSC-2: AIR GAP AROUND MDF EXPLOSIVE SOURCE

MP-6700-28

FIGURE 22 CRACK PATTERNS PRODUCED IN SPRINGING EXPERIMENTS

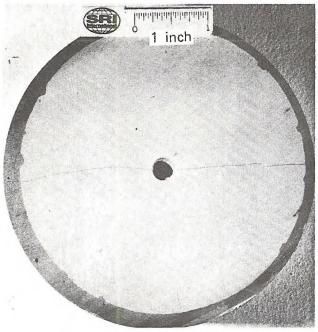

(a) SECTION 1/2 INCH FROM DETONATION POINT

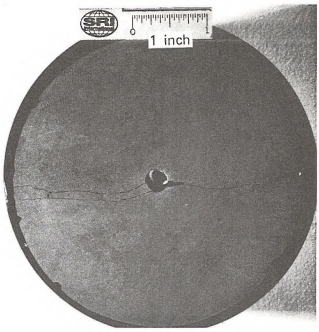

(b) SECTION 2-1/8 INCHES FROM DETONATION POINT

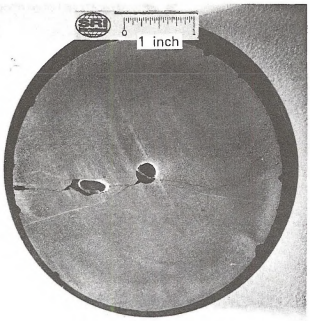

(c) SECTION 3-1/4 INCHES FROM DETONATION POINT

(d) SECTION 4-3/8 INCHES FROM DETONATION POINT

MP-6700-35

FIGURE 23 SECTIONS THROUGH DEVONIAN SHALE CYLINDER GSC-2

Scale is in inches.

interval. The widths of the zones in each section were approximately equal. The zone nearest the borehole showed the most damage. The crack lengths were determined from photographic maps of each section, made at a magnification of approximately 6.2; actual crack lengths slightly less than 0.5 mm could be resolved and counted with this procedure. Only one crack orientation, radial, was used, and all cracks counted were assumed to be radial. However, this procedure could be extended to include other orientations, thus allowing smaller angular variations to be determined.[5]

A weighting scheme was used to determine the number of cracks within each length and orientation interval. If a crack was wholly within a zone, not touching the zone boundaries, it was counted as one crack in the appropriate interval. If it did not intersect the borehole but crossed n boundaries, it was weighted by the fraction $\frac{1}{(n+1)}$. If the crack intersected the borehole and n boundaries, it was weighted by $\frac{1}{2(n+1)}$, and its length was doubled. Thus, a crack of length L that crossed one zone boundary but did not intersect the borehole was counted as 1/2 crack of length L in each of the two zones. If the crack of length L intersected the borehole and one other zone boundary, it was counted as $\frac{1}{2\times 2}$, or one-fourth, of the crack of length 2L. Finally, the crack size distribution for each zone was expressed as the cumulative crack density (i.e., the number of cracks per unit surface area greater than a given radius) versus the crack radius (which was assumed to be one-half the crack length).

The radial crack size distributions from the two laboratory experiments are shown in Figure 24. These surface crack data were then converted with the BABS2 statistical transformation[7] to volume counts, shown in Figure 25.

3. Analysis

The results of experiments GSC-1 and GSC-2 were used to derive the fracture parameters for Devonian shale used in the final parameter sensitivity analyses.

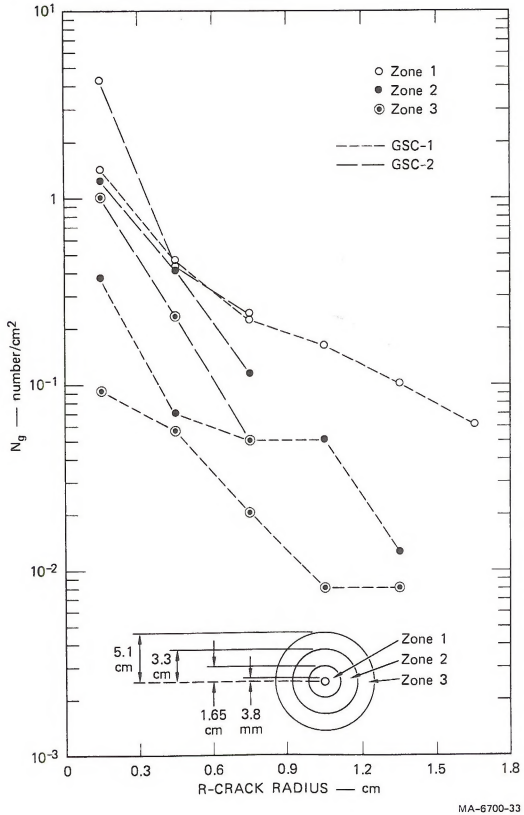

FIGURE 24 AREA CUMULATIVE RADIAL CRACK SIZE DISTRIBUTIONS FOR THE TWO DEVONIAN SHALE SPRINGING EXPERIMENTS (GSC-1, GSC-2)

Inset shows zone positions and dimensions.

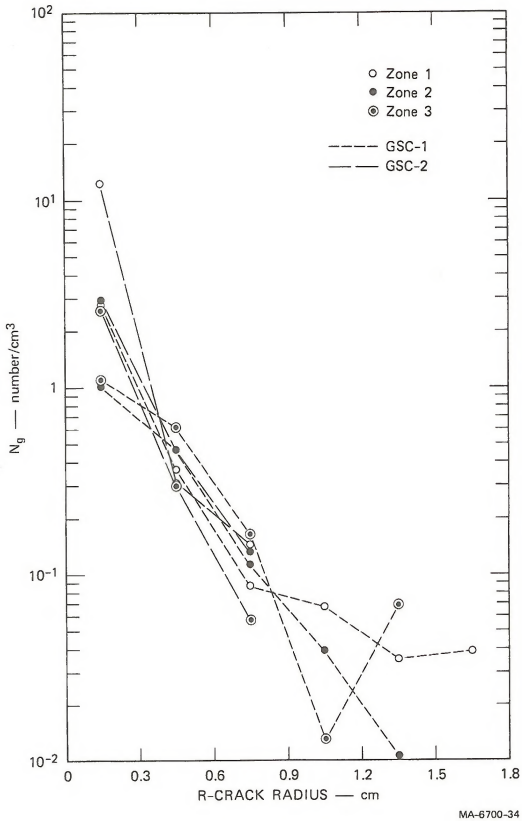

FIGURE 25 VOLUME CUMULATIVE RADIAL CRACK SIZE DISTRIBUTIONS
Data taken from Figure 24.

Table 5 summarizes the data on the radial crack size density distribution parameters shown in Figure 25. It was assumed* the crack size data fit the distribution for penny shaped cracks given by Equation 1:

$$N_R = N_o \exp(-R/R_1).$$

The values of N_o and R_1 for each zone in both experiments were determined by visually fitting a straight line to the data (Figure 25) and noting its intercept and slope (Table 5).

To determine a set of fracture parameters from NAG-FRAG that reproduced these experimental results, we incorporated NAG-FRAG into the one-dimensional wave propagation code PUFF.[13] The cylindrical geometry used to represent the experiments is shown in Figure 26. The material parameters for Devonian shale used throughout these calculations are given in Table 2, and the initial set of fracture parameters are given in Table 1 (GS-4). The input pressure history used in these calculations was taken from the borehole stress gage measurements (Ex 1) in experiment GSC-1 (Figure 21).

Figure 27 shows a comparison of the stress histories from experiment GSC-1, which were used to constrain the calculations, and the predicted stress histories. Because the stress gages operated for less than 10μs (but the calculations continue beyond 10μs), it was necessary in the calculations to allow the input pressure to decay in an arbitrary manner, as indicated by the decaying compression shown in Figure 27 for Ex 1 (F5 and F10). The predicted stress wave arrival time at gage A-2 (Figure 27) does not match the observations because two-dimensional effects occurred in the experiment that were not modeled in the calculations. For example, although zero time is taken to be the time of detonation of the explosive in the experiments, the detonation was not simultaneous but ran from bottom to top (Figure 19). Thus, the arrival time at gage A-2 is earlier in the calculations than in the experiments. Nevertheless, the predicted peak stresses are in good agreement, suggesting that the predicted damage gradients should not be grossly distorted by the one-dimensional geometry used.

The initial set of fracture parameters (Table 1, GS-4) were then iterated until the predicted radial crack size density distributions were comparable to those observed, within the

*Assumption is suggested by data given in Appendix A.

Table 5

COMPARISON OF OBSERVED TO PREDICTED RADIAL CRACK SIZE DENSITY DISTRIBUTION PARAMETERS

	Observed				Predicted*			
	Experiment GSC-1		Experiment GSC-2					
Zone	N_o(no./cm^3)	R_1(cm)	N_o(no./cm^3)	R_1(cm)	N_o(no./cm^3)		R_1(cm)	
1	2.8	0.20	7.6	0.13	10.4†	24.3‡	0.24†	0.15‡
2	1.0	0.30	2.7	0.19	1.52	1.42	0.19	0.38
3	1.1	0.30	2.4	0.16	0.29	0.43	0.03	0.07

*These values were predicted using NAG-FRAG in the one-dimensional wave propagation code PUFF with a cylindrical geometry (Figure 26).

†Calculation designation: F5 - Input (borehole) pressure history in calculation identical to borehole pressure history in Experiment GSC-1 for $0 \leq t \leq 8.9$ μs followed by an exponentially decaying pressure history to 30 μs (Figure 27). These are the values of N_o and R_1 at t = 30 μs (Figure 28).

‡Calculation designation: F10 - Input (borehole) pressure history in calculation identical to borehole pressure history in experiment GSC-1 for $0 \leq t \leq 8.9$ μs followed by an expontentially decaying pressure history to $P(t) = 10^5$ dyn/cm^2 at t = 50 μs (Figure 27). These are the values of N_o and R_1 at t = 50 μs (Figure 28).

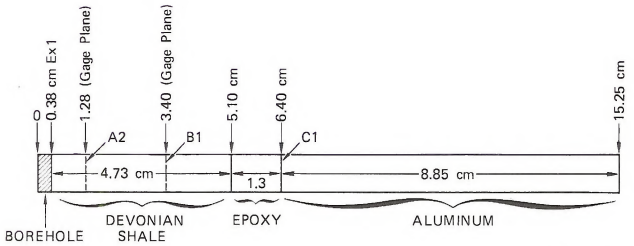

FIGURE 26 CONFIGURATION USED IN ONE-DIMENSIONAL CYLINDRICAL GEOMETRY CALCULATIONS TO DETERMINE FRACTURE PARAMETERS OF DEVONIAN SHALE

Layout reproduces experiment GSC-1 (Figure 18).
Stress gage positions shown from GSC-1.

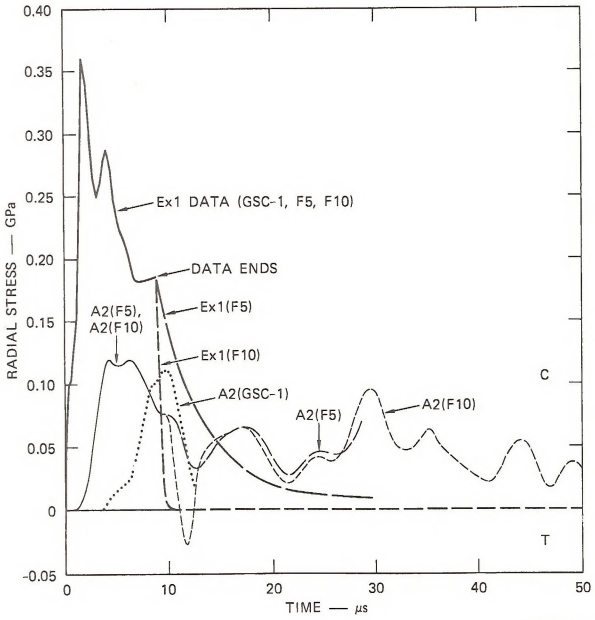

FIGURE 27 COMPARISON OF RADIAL STRESS HISTORIES FROM EXPERIMENT GSC-1 AND CALCULATIONS F5 AND F10

Ex1 is the borehole stress gage position.
A2 is an in-material stress gage (see Figure 26).
C = compression, T = tension.

limits of the NAG-FRAG model. The parameters that gave the best agreement are shown in Table 6, and the predictions are compared to the observations in Table 5. The experimental crack distributions (Figure 25) are replotted in Figure 28 with the predicted distributions (Table 5) superimposed for comparison.

Although the total crack density (N_u) is relatively unaffected by the decay rate of the pulse (or total pulse duration), the characteristic crack size (R_1) is dependent on the pulse duration (Figure 28): cracks will grow in response to the applied compressive "tail" of the input pressure. The ringing (oscillating stress) at gage position A-2 in calculations F5 and F10 demonstrates that the small sample size will allow multiple tensile pulses to propagate through the sample, and hence the crack sizes will increase during each pulse. In addition, the small sample size does not allow an accurate determination of the crack size density distribution at large crack sizes.

Thus, in either case there is some uncertainty about both the experimental value of R_1 and the relationship of the predicted large crack sizes (e.g., much greater than the computational cell dimension) to those observed. Nevertheless, the fracture parameters in Table 6 result in fairly good agreement between the predicted and observed total radial crack density (N_u) and the crack density distributions at small crack radii (e.g., R < 1 cm).

Although the overall features of the experimental distributions have been reproduced, the predicted damage gradient is larger than observed. Some possible reasons for this discrepancy are:

- two-dimensional effects are not included in these calculations.
- shear cracking effects (discussed in Reference 5) are not included.
- the material model and parameters for Devonian shale may be in error.
- the method for counting cracks in a cylindrical geometry may be incorrect.

The last possibility may be responsible for the smallness of the observed damage gradient. If a radial crack in the shale is not linear (i.e., if its orientation changes), it will be counted as several small cracks in the counting scheme. In an extreme case, if a radial crack is initiated at the borehole and propagates to the shale boundary but changes its orientation, "jogs" as it propagates, each segment will be weighted as an individual crack. This results in a smaller

Table 6

FRACTURE PARAMETERS USED IN
FINAL ANALYSES FOR DEVONIAN SHALE
(Calculation Designation: F5)

Parameter	Numerical Values	Dimensions
Growth coefficient, $\frac{1}{4\eta}$, T_1	-8.0×10^{-4}	$cm^2/dyn\text{-}sec$
Growth threshold stress, σ_{go}, T_2	-5.0×10^{6}	dyn/cm^2
Nucleation size parameter, R_1, T_3	8.0×10^{-3}	cm
Nucleation rate coefficient, $\dot{N}_o$, T_4	3.0×10^{4}	$\frac{number}{cm^3\text{-}sec}$
Nucleation threshold stress, σ_{no}, T_5	-1.0×10^{8}	dyn/cm^2
Stress sensitivity factor, σ_1, T_6	-7.5×10^{7}	dyn/cm^2
Upper size cutoff for nucleation, T_7	5.1	cm
Threshold stress for entering subroutine, T_8	0.0	dyn/cm^2
Ratio of number of fragments to number of cracks, T_{10}	3.3×10^{-1}	--
Ratio of fragment radius to crack radius, T_{11}	1.0	--
ΣNR^3 at coalescence, T_{12}	0.2	--
Coefficient for calculating fragment volume, T_{13}	5.0×10^{-2}	--

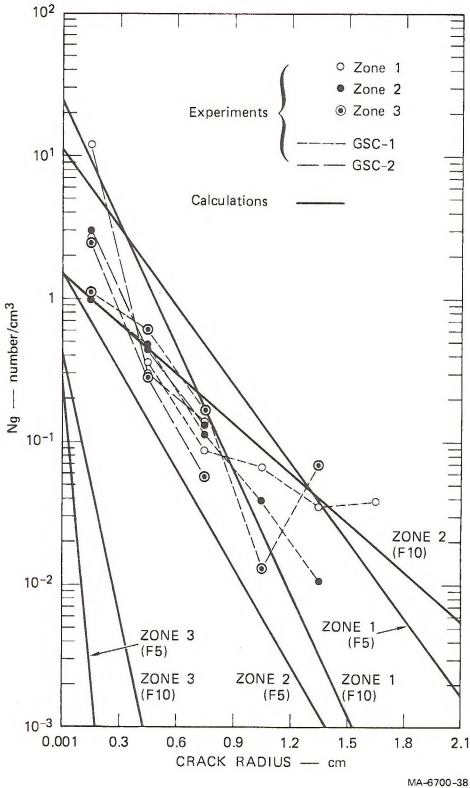

FIGURE 28 COMPARISON OF RADIAL CRACK SIZE DENSITY DISTRIBUTIONS FROM EXPERIMENT GSC-1 AND GSC-2 TO NAG-FRAG PREDICTIONS

Fracture parameters in Table 6 used for the calculations indicated in Table 5.

observed damage gradient and may severely affect the analysis when large cracks predominate, as they did in these experiments, (Figures 22 and 23).

Although this crack counting scheme may be inappropriate at low crack densities, it does have the advantage of not requiring subjective decisions about where the crack nucleated or its direction of propagation. In the calculations, this problem is avoided because each computational cell is assigned its own distribution, and the largest crack size may be larger than the cell size.

In spite of the limitations, these fracture parameters (Table 6) do reproduce both total crack density (N_n) and characteristic crack size (R_1) reasonably well in the first two zones.

E. Summary

The Devonian shale was characterized in terms of its bulk material properties and fracture characteristics. The measured bulk properties are listed in Table 3. The microstructure of the shale prior to the experiments was found to be relatively homogeneous but rubblelike, suggesting that fracture would occur between grains; this was confirmed by examination of the shale after the experiments (Figures 16 and 17). The NAG-FRAG fracture parameters (Table 6) were determined by matching the predicted crack size density distributions to those observed in experiments GSC-1 and GSC-2, and by iterating the parameters until suitable agreement was obtained. Although the observed damage gradient was not reproduced, the predicted total crack density and characteristic crack size in zones 1 and 2 match the observations reasonably well (Table 5).

VII FINAL FRACTURE PARAMETER SENSITIVITY ANALYSIS

A. Introduction

The objectives of the fracture parameter sensitivity analysis were to:

- Determine the sensitivity of the computed crack density distributions to variations in the model parameters and hence, ascertain the effect of natural material property variations on crack densities.
- Provide a data base for later comparison with computations of crack densities produced by different input pressure histories (i.e., to differentiate between crack density distributions produced by variations in material properties and by changes in the input pressure history).

For this analysis, NAG-FRAG was used in conjunction with PUFF[13] to model the interaction of the stresses with the material response.

The constitutive relations and material properties used to model the Devonian shale in the final fracture parameter sensitivity analysis were those used in the preliminary analysis (see Section V).

B. Final Fracture Parameter Sensitivity Analysis

The fracture parameters T_1 and T_4 were varied for different pulse shapes (Table 7). The computations were performed for the cylindrical geometry shown in Figure 29(a), using NAG-FRAG in conjunction with PUFF and the input pressure histories (discussed in detail in Section VIII) shown in Figure 29(b). The starting fracture parameters used are given in Table 6.

Figure 30 shows that the distribution of total crack density (N_o) as a function of radius is essentially the same for identical pulse shapes; only the magnitude of N_o varies. Thus, the material property variations, within the range of values examined, alter the total number of cracks produced. (The length of the cracks may also be varied in a manner that is uniform with distance from the borehole, as discussed in Section VI.D.)

Table 7

PARAMETERS USED IN PULSE SHAPING CALCULATIONS*

Calculation Designation	$\tau(\times 10^{-6}$ sec)	T_1 $\frac{cm^2}{dyn\text{-}sec}$	T_4 $\frac{number}{cm^3\text{-}sec}$
PS144	1.00	-8.00×10^{-4}	3.00×10^{4}
PS544	5.00	-8.00×10^{-4}	3.00×10^{4}
PS1044	10.00	-8.00×10^{-4}	3.00×10^{4}
PS145	1.00	-8.00×10^{-4}	3.00×10^{5}
PS545	5.00	-8.00×10^{-4}	3.00×10^{5}
PS1045	10.00	-8.00×10^{-4}	3.00×10^{5}
PS134	1.00	-8.00×10^{-3}	3.00×10^{4}
PS534	5.00	-8.00×10^{-3}	3.00×10^{4}
PS1034	10.00	-8.00×10^{-3}	3.00×10^{4}

*Input radial stress history: $P(t) = \frac{1}{\tau} \text{MAX}(e^{\frac{-t}{\tau}}, 0.1)$GPa for $t \geq 0$.

All other fracture parameters used in these calculations have the values shown in Table 6.

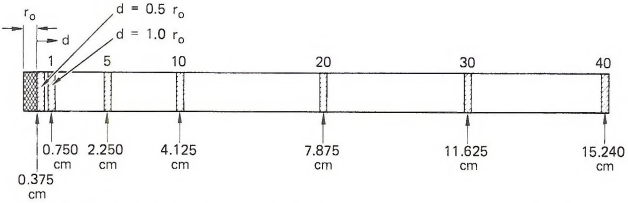

(a) CONFIGURATION USED IN ONE-DIMENSIONAL CYLINDRICAL GEOMETRY

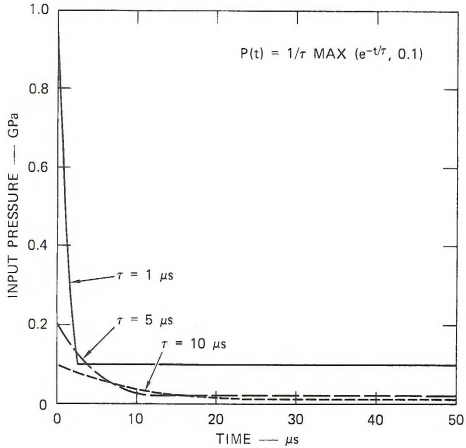

(b) INPUT PRESSURE HISTORY

MA-6700-41

FIGURE 29 CONFIGURATION AND INPUT PRESSURE HISTORY USED IN ONE-DIMENSIONAL CYLINDRICAL GEOMETRY PULSE SHAPING CALCULATIONS

r_o is the borehole radius, and d is the distance of the computational cell from the borehole boundary in units of r_o. τ is the pulse width.

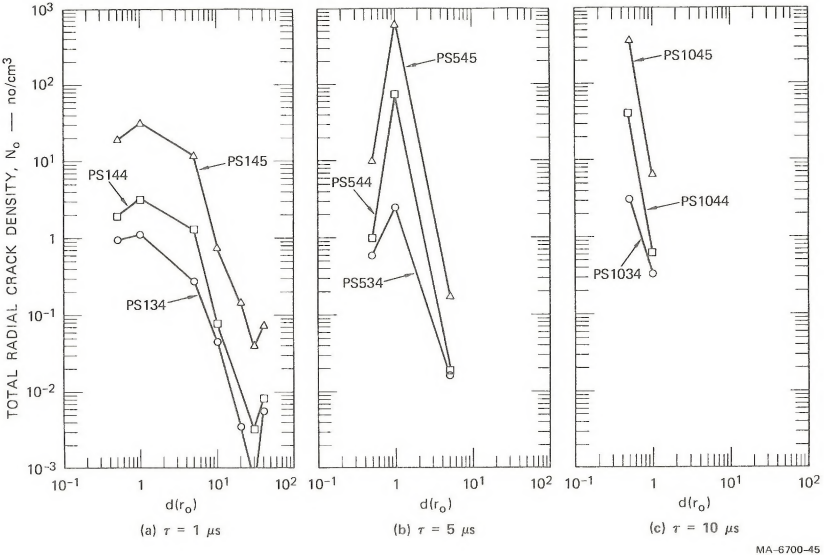

FIGURE 30 DAMAGE GRADIENTS FROM THE PULSE SHAPING CALCULATIONS: EFFECT OF MATERIAL PROPERTY VARIATIONS

The data plotted in Figures 31 and 32 show the variation in N_o as a function of T_1 and T_4 for the different pulse shapes, at different distances from the borehole. These data show that an order of magnitude increase in T_1 will decrease N_o by a factor of from 2 to 10. The steepest declines in N_o for an order of magnitude increase in T_1 are for the 10 μs pulse width at d = $0.5r_o$ and for the 5 μs pulse width at d= $1.0r_o$. However, an order of magnitude increase in T_4 causes a nearly order of magnitude increase in N_o for any specific pulse shape. The magnitude of N_o depends both on the distance from the borehole and the pulse width.

C. Conclusions

The final parameter sensitivity analysis demonstrated that the total radial crack density (N_o) is dependent on the pulse width (τ) and the distance of the material from the borehole (d), as well as on the fracture parameters. At a constant value of τ and d, the crack density (N_o) tends to decrease with increasing values of the growth coefficient (T_1), but it increases with increasing values of the nucleation rate (T_4). In general, an order of magnitude increase in T_1 will cause N_o to decrease by a factor of from 2 to 10, but an order of magnitude increase in T_4 will cause an order of magnitude increase in N_o. Therefore the crack density produced in Devonian shale will depend strongly on the material properties of the shale, but the rate of the variation of N_o with distance (d) is relatively unaffected by the fracture parameters.

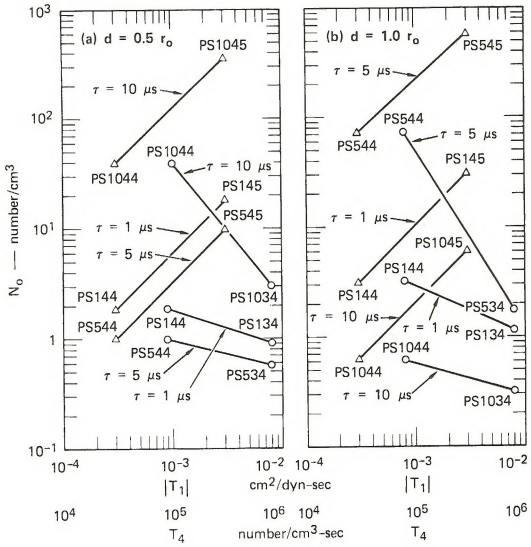

FIGURE 31 TOTAL RADIAL CRACK DENSITY (N_o) FOR VARIATIONS IN FRACTURE PARAMETERS (T_1,T_4) AND PULSE DURATION (τ) AT 0.5 AND 1.0 BOREHOLE RADII

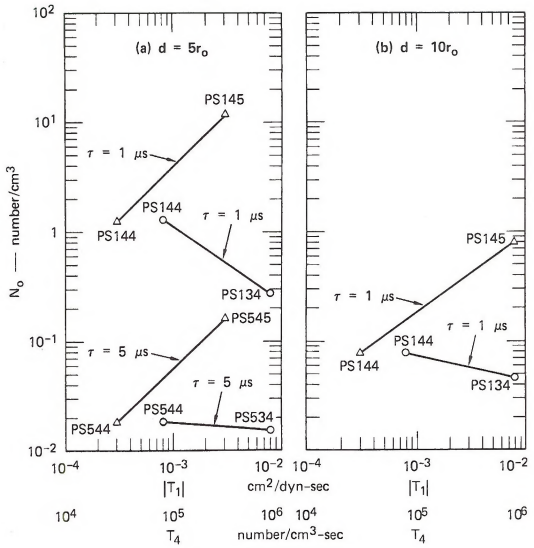

FIGURE 32 TOTAL RADIAL CRACK DENSITY (N_o) FOR VARIATIONS IN FRACTURE PARAMETERS (T_1,T_4) AND PULSE DURATION (τ) AT 5.0 AND 10.0 BOREHOLE RADII

VIII FINAL PULSE SHAPING SENSITIVITY CALCULATIONS

A. Introduction

After performing the preliminary calculations, determining the values of the fracture parameters appropriate to Devonian shale and the sensitivity of the fracture density to variations in the parameters, we performed a final series of pulse shaping calculations to examine the effect of changes in input pressure history on the crack size density distribution, i.e., to determine feasabiltiy of pulse-tailoring. The final series of pulse shaping calculations differed from the preliminary ones in several ways.

First, the input pressure history function was changed as in the parameter sensitivity analysis to allow arbitrary waveforms to be specified rather than being limited to the function specified by the equation of the state of PETN and the resultant expansion of the explosive chamber (borehole). This permitted more direct evaluation of the role of pulse shape: parameters characterizing the pulse shape could be varied independently.

Second, we performed one damage (fracture) and two no-damage calculations with fixed peak input pressures and varying pulse widths to examine the effect of pulse width on the resultant radial and circumferential stress, and also the effect of damage on these stresses. For these and subsequent calculations, a single pulse shape was chosen that could be uniquely characterized by its duration. An exponential function was selected for the decay because it provides a simple, smooth, pressure decay of width determined by the time constant, τ:

$$P(t) = \frac{1}{\tau} \max\left[e^{-\frac{t}{\tau}}, 0.1\right] GPa, \; t \geqslant 0 \tag{8}$$

where t is the time from detonation in microseconds. In addition to meeting the above criteria, this pulse shape was similar to that observed in the springing experiments and to those of previous calculations and experiments in oil shale.[5] It was also intended that this shape would allow the impulse to be held constant for different widths. We considered that if different crack density distributions were produced by pulse shapes of the same impulse, then the pulse tailoring concept would be verified. However, as described below, it was not possible to keep the impulse constant.

B. Pulse Width Calculations

The results illustrating the effect of pulse width as predicted by PUFF and NAG-FRAG (for the one-dimensional cylindrical geometry shown in Figure 29a) are shown in Figures 33, 34, and 35. The fracture parameters (and material properties, Table 2) are those of Table 7 for the calculation designated PS144. In Figure 33 are shown the radial stress histories at a radius of d = 2.5 r_a for three cases, one with τ equal 5 μsec and no damage allowed, i.e., the NAG-FRAG subroutine was not called; one of equal duration with damage; and one of no damage but $\tau=\infty$. The primary features are evident from the figure. First, at this radius, the damage, i.e., radial fracture, has little effect on the radial stress history. This is also true at other radii (not shown). Second, even though the input pressure in one case is of infinite duration, the radial stress history is not grossly different from that produced by the narrow pulse. At larger distances, there is even less difference. Therefore the pulse shape and damage are not significantly affecting the radial stress histories.

By contrast, the circumferential stresses at this distance are greatly modified by the borehole pulse shape as seen in Figure 34. Although the tensile stress amplitude is approximately the same at this radius, the duration is considerably increased for the $\tau=\infty$ pulse. This relationship is maintained for all radii except very near the borehole, where the $\tau=\infty$ pulse produces very low amplitude tensile stress, and the narrow pulse produces large tensile stress, as shown in Figure 35. This condition is perhaps caused by a large compressive radial stress maintained in this region by the wide pulse, whereas the radial stress goes tensile with a narrow pulse.

The effects of NAG-FRAG on the circumferential stresses are also shown in Figures 33, 34, and 35. It can be seen that, in general, the stresses are modified as though there were a time dependence, i.e., fracture is initiated during the increase in tensile stress (not shown, but discussed in Section VIII.C), whereas the resulting stress relaxation occurs considerably later. In the fracture subroutine, the applied tensile stress, σ of equations 2 and 3, is reduced as the fracture density, N_0, and crack size, R_1, increase, according to $N_0 R_1^3$. Thus the fracture damage is coupled to the reduction in applied tensile stress by both the number of cracks and crack size.

A more detailed analysis of the effect of damage was not possible, because the pulse widths in the two cases were not strictly identical. Specifically, it was found necessary to add a compressive tail to the narrow pulses to prevent the calculations from indicating multiple-crack

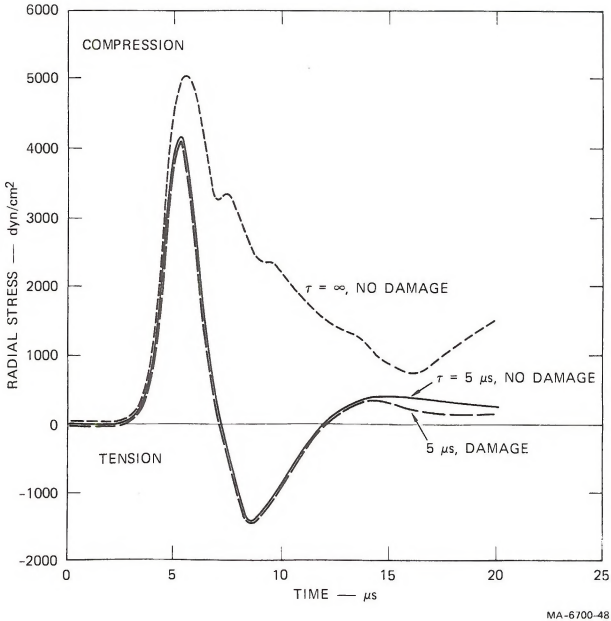

FIGURE 33 RADIAL STRESS HISTORIES AT DISTANCE $d = 2.5r_o$ (SEE FIGURE 29) FOR DIFFERENT INPUT PRESSURE HISTORIES

τ is the width of input pulse.

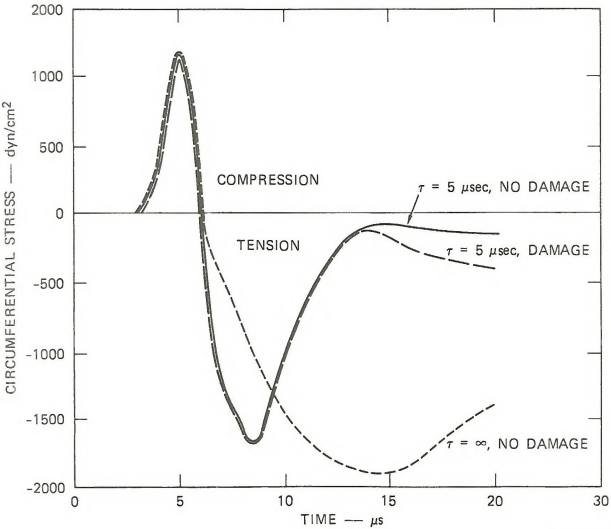

FIGURE 34 CIRCUMFERENTIAL STRESS HISTORIES AT DISTANCE $d = 2.5r_o$ (SEE FIGURE 29) FOR DIFFERENT INPUT PRESSURE HISTORIES

τ is the width of input pulse.

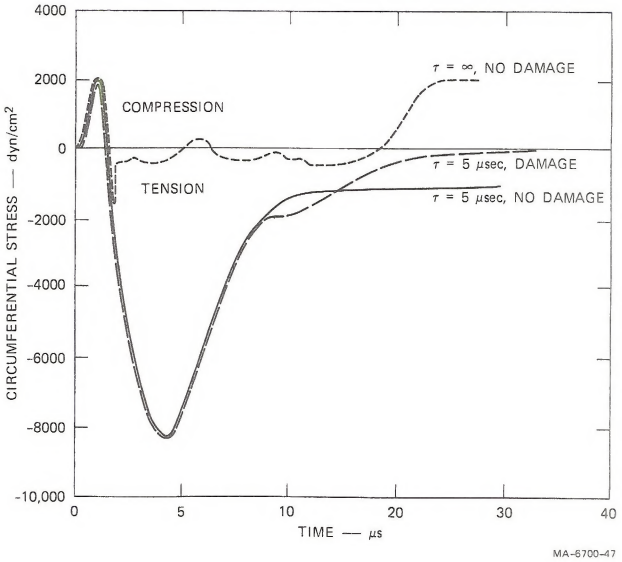

FIGURE 35 CIRCUMFERENTIAL STRESS HISTORIES AT A DISTANCE $d = 0.3r_o$ (SEE FIGURE 29) FOR DIFFERENT INPUT PRESSURE HISTORIES

opening and closing with resultant numerical instabilities. As discussed below this necessary procedure precluded our performing constant impulse calculations.

The major conclusion from the pulse width calculations at constant input amplitude is that the tensile, circumferential stress history is strongly pulse shape dependent. To the extent that the input pulse shape controls the circumferential stress history, the fracture distributions should be dependent on that input pulse shape.

C. Fracture Density Dependence

Three calculations were performed in which the pulse amplitude and widths were varied. As mentioned, the initial intent was to maintain constant impulse to the borehole wall. However, the small compressive tail necessary for calculational stability prevented our adjustment of impulse by the one parameter, τ. We therefore calculated damage as a function of the three pulse widths and amplitude combinations shown in Figure 29(b).

The one-dimensional, cylindrical geometry and the input pressure histories are shown in Figure 29(a) and 29(b), respectively. The cell locations are given in centimeters and in multiples of the borehole radius, r_w. As in the prior calculations, the pulse shape for the exponentially decreasing portion of the profile is given by Equation 8. PUFF[13] was used in the wave propagation calculations and the NAG-FRAG subroutine to calculate damage. The fracture parameter and τ variations are given by values in Table 7. It can be seen from Figure 29(b) that although the impulse of the exponential portions are equal, the compressive tails nullify the constant impulse feature at late times. However, the nonconstant impulse does not alter the conclusions.

The damage predicted by the calculations is listed in Table 8 as the total radial crack density, N_a, and the characteristic radial crack size, R_1, at various distances and conditions of Table 7. The stress and crack density histories at two radii, 1 r_w, and 10 r_w, are shown in Figure 36. It is difficult to form general conclusions from these data because the fracture parameters, i.e., nucleation, T_4, and growth rate, T_1, interact with the tensile stress history and stress relaxation, which depend on $N_a R_1^3$. However, specific observations can be made. From Figure 36 it can be seen that the total crack density rapidly reaches a maximum at any given location and remains constant until the reflected stress (from the sample boundary) reaches the computational cell. Table 8 illustrates that the crack size, R_1, increases slowly, which may be due to the

Table 8

COEFFICIENTS OF RADIAL CRACK SIZE DENSITY DISTRIBUTIONS AT VARIOUS DISTANCES

d^* (r_o)	d (cm)	N_o (no./cm^3)	R_1 (cm)	N_o (no./cm^3)	R_1 (cm)	N_o (no./cm^3)	R_1 (cm)
		PS144		PS544		PS1044	
0.5	0.375	1.9×10^{0}	1.9×10^{-2}	1.0×10^{0}	1.4×10^{-2}	4.0×10^{1}	$^{\bullet}1.6 \times 10^{-1}$
1	0.750	3.2×10^{0}	2.0×10^{-2}	7.3×10^{1}	$^{\bullet}1.5 \times 10^{-1}$	6.1×10^{-1}	$^{\bullet}1.4 \times 10^{-1}$
5	2.250	1.3×10^{0}	$^{\bullet}5.3 \times 10^{-1}$	1.9×10^{-2}	$^{\bullet}1.9 \times 10^{-2}$	0	0
10	4.125	$^{x}7.8 \times 10^{-2}$	$^{\bullet}9.1 \times 10^{-2}$	0	0	0	0
20	7.875	$^{x}1.3 \times 10^{-2}$	$^{\bullet}1.9 \times 10^{-2}$	0	0	0	0
30	11.625	3.2×10^{-3}	$^{\bullet}1.5 \times 10^{-2}$	0	0	0	0
40	15.240	8.2×10^{-3}	$^{\bullet}1.0 \times 10^{-2}$	0	0	0	0
		PS134		PS534		PS1034	
0.5	0.375	9.4×10^{-1}	6.7×10^{-1}	5.8×10^{-1}	6.7×10^{-1}	3.07	4.7×10^{-1}
1	0.750	1.13	6.3×10^{-1}	2.47	5.1×10^{-1}	3.3×10^{-1}	9.9×10^{-1}
5	2.250	2.8×10^{-1}	1.05	1.6×10^{-2}	2.37	0	0
10	4.125	4.6×10^{-2}	1.91	0	0	0	0
20	7.875	3.5×10^{-3}	$^{\bullet}5.34$	0	0	0	0
30	11.625	0	$^{\bullet}0$	0	0	0	0
40	15.240	5.6×10^{-3}	$^{\bullet}1.02$	0	0	0	0
		PS145		PS545		PS1045	
0.5	0.375	1.9×10^{-1}	1.9×10^{-2}	1.0×10^{1}	1.4×10^{-2}	3.6×10^{2}	$^{\bullet}8.1 \times 10^{-2}$
1	0.750	3.2×10^{1}	2.0×10^{-2}	6.0×10^{-2}	$^{\bullet}7.6 \times 10^{-2}$	6.3×10^{0}	$^{\bullet}1.4 \times 10^{-1}$
5	2.250	1.2×10^{1}	$^{\bullet}2.6 \times 10^{-1}$	1.7×10^{-1}	$^{\bullet}2.0 \times 10^{-2}$	0	0
10	4.125	$^{x}7.8 \times 10^{-1}$	$^{\bullet}1.0 \times 10^{-1}$	0	0	0	0
20	7.875	$^{x}1.5 \times 10^{-1}$	$^{\bullet}1.9 \times 10^{-2}$	0	0	0	0
30	11.625	4.2×10^{-2}	1.5×10^{-2}	0	0	0	0
40	15.240	7.7×10^{-2}	1.1×10^{-2}	0	0	0	0

*d is the distance of the computational cell from the center of the borehole. r_o is the borehole radius.

•R_1 is still increasing at end of computations (t=50μs); value is lower bound.

x value of N_o before arrival of reflected wave.

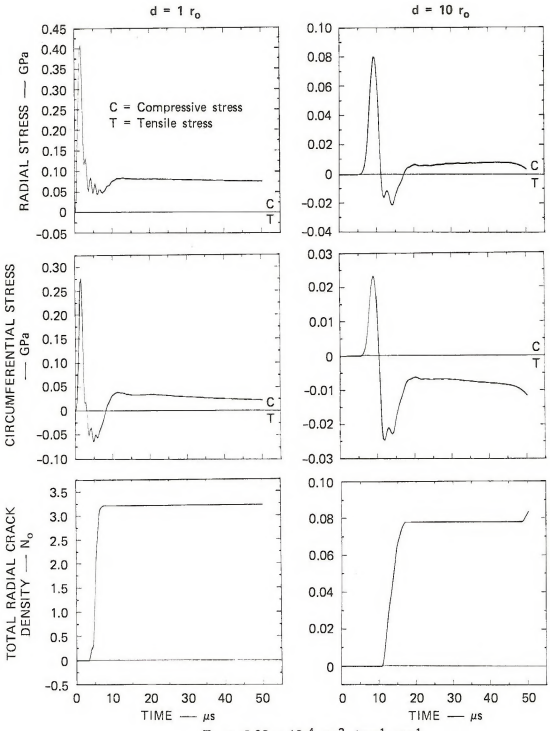

FIGURE 36 STRESS AND DAMAGE DISTRIBUTIONS AT 1 AND 10 BOREHOLE RADII
(Calculation PS144, Table 7)

compressive tail added to the input pulses. Also from Table 8 it can be observed that in general, the crack density varies approximately as expected for a small density of large cracks in cylindrical geometry.

D. Conclusions

More general and significant conclusions can be drawn by comparing N_a versus radius for the three pulses and as a function of the fracture parameters, T_1 and T_4, as shown in Figure 37. The relative numbers of cracks as a function of radius do not depend on the fracture parameters, i.e., the shapes of the plots do not change indicating a dependence on pulse shape only. It should be noted that the durations shown in Figure 37 refer only to the exponential part of the pulse, whereas the computed damage is a result of the total pulse duration. The fracture parameters significantly affect the total radial crack density, and therefore, to predict crack density requires that the fracture parameters be determined.

The pulse shape variations used in these calculations were very limited. The results indicate a strong pulse shape sensitivity but do not permit conclusions of the individual effects of durations, amplitudes, and the rates of borehole loading and unloading.

The results of our work on fracture calculations using NAG-FRAG have indicated several areas where improvement in current fracture codes is required. Specifically, present codes do not treat shear cracking, which in cylindrical geometry of the borehole studies appears to be a possible major source of crack production close to the borehole. Also, present codes, including NAG-FRAG, experience instabilities when treating crack closure and reopening. In our work, this problem was overcome after considerable anguish by adding a compressive tail to the input pulse to prevent crack closing. However, the specific effect of this procedure is not clear because, as indicated, the relationship between the borehole compressive stress and the radial and circumferential stress in the material is dependent on many factors, including fracture density, size, and stress relaxation propagation. Additional model development is therefore required to adequately treat both shear cracking and crack closure.

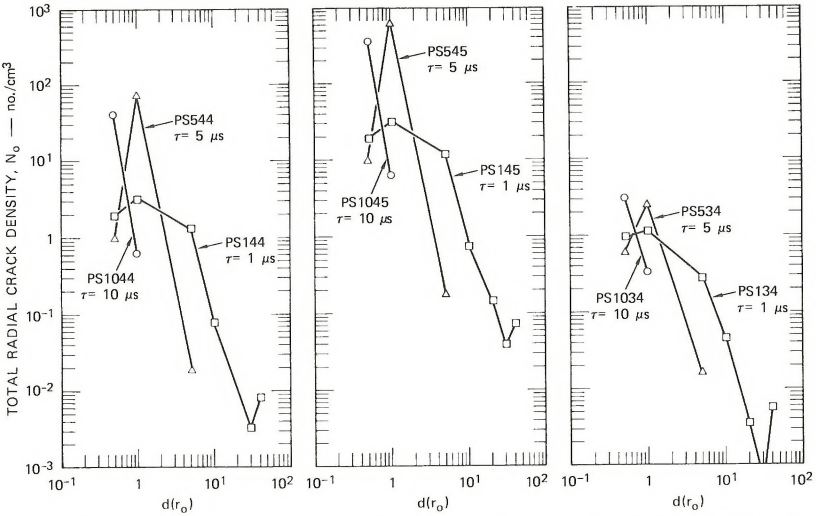

(a) $|T_1|$ = 8.00 x 10^{-4} cm^2 dyn^{-1} sec^{-1}
T_4 = 3.00 x 10^4 no. cm^{-3} sec^{-1}

(b) $|T_1|$ = 8.00 x 10^{-4} cm^2 dyn^{-1} sec^{-1}
T_4 = 3.00 x 10^5 no. cm^{-3} sec^{-1}

(c) $|T_1|$ = 8.00 x 10^{-3} cm^2 dyn^{-1} sec^{-1}
T_4 = 3.00 x 10^4 no. cm^{-3} sec^{-1}

MA-6700-44

FIGURE 37 DAMAGE GRADIENTS PRODUCED BY INDICATED FRACTURE PARAMETERS (T_1,T_4) AND "PULSE DURATIONS" (τ)

APPENDIX
BOREHOLE STRESS GAGE EXPERIMENTS

A. Introduction

An important aspect of fracture research is to assess the role of the explosive pulse shape in the fracture pattern produced in the shale. This assessment required experiments, quantification of the resulting crack patterns, and computer simulations to compare predictions with the experiments (Section VI.D).

Since one of the factors in the calculations is the shape of the stress pulse produced in the shale by the explosive, it is desirable to make stress-time measurements as close as possible to the interface between the explosive and the shale. However, it is also desirable to have a means of verifying our calculated values of stress within the samples, because fracture damage is determined from these values. The value of such measurements is demonstrated by the unexpectedly low stress observed in experiment GSC-1, for which calculations had indicated a value considerably higher.

The major problem is to make the gages survive long enough to record the stress wave introduced into the shale. To accomplish this, we performed several experiments using manganin[16] and ytterbium stress gages[17] placed at the interface between an explosive and a solid.* After perfecting the technique for recording the stress-time profile at this interface, we performed the springing experiments (Section VI).

B. Results

Experiment 1: PETN in Steel Pipe, Maganin Gage

The arrangement for the borehole stress gage experiments is shown in Figure A-1. A four-lead (two for voltage, two for current), T-shaped manganin stress gage (1 mm x 5 mm) was mounted between layers of Kapton** and placed inside a metal pipe (approximately 6.5 mm I.D., 10.3 mm O.D., 20 cm long) to simulate a borehole. Kapton is a tough polymer and a good electrical insulator. PETN was pressed into a soda straw (approximately 6.0 mm diameter) at a density of 0.6 g/cm^3 (total weight, 3.5 gm), and a bridgewire detonator was attached to one end of the straw. The straw was inserted into the pipe so that the gage package (0.5 mm

*Details of gage constructon and use are given in references 16 and 17.

**Trademark for DuPont polyimide plastic.

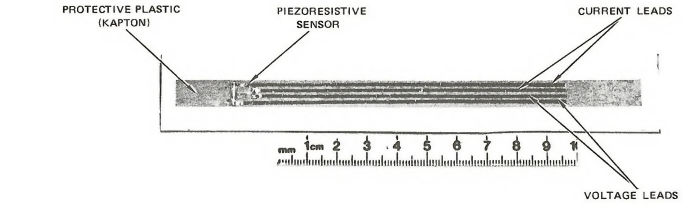

(a) STRESS GAGE MOUNTED ON KAPTON

(b) STRESS GAGE SANDWICHED BETWEEN
KAPTON LAYERS AND INSERTED IN PIPE

MP-6700-6

FIGURE A-1 EXPERIMENTAL CONFIGURATION TO TEST SURVIVABILITY OF STRESS GAGES

thick) was between the straw and the inner wall of the pipe. Between the stress gage and the PETN, there was a 0.20 mm thick layer of Kapton. Between the gage and the pipe wall, there was a 1.02 mm thick layer. The Kapton layer between the gage and the PETN served to protect the gage for a short time after detonation.

The stress gage signals were recorded by oscilloscopes (see Figure A-2). The signals were so noisy, apparently because of the stress wave reverberating in the pipe, that the data were not reduced. However, the peak pressure recorded was about 1.5 GPa, and the pulse duration was about 1 to 3 μs (see Table A-1). These results indicated that the gages could operate satisfactorily, but that better signal-to-noise ratios would be required to obtain useful data. Therefore, the next set of experiments was performed with the addition of more sensitive ytterbium sensors. In addition, thicker cylinders were used to eliminate the reverberations in stress.

Experiments 2 and 3: PETN in a Lucite Cylinder, Manganin Gage

In these two experiments, a thick-walled lucite cylinder (7.1 mm I.D., 5.1 cm O.D., 20 cm long) was used instead of the pipe. The configuration was the same as in Experiment 1. The explosive source was again PETN (0.6 g/cm^3). The data are shown in Figure A-2. Again the signals were noisy, with severe stretching of the manganin gage about 3 μs after the stress-wave arrival, so we did not reduce the data. However, the peak pressure and pulse duration were about 1.5 GPa and 1 to 3 μs (Table A-1).

Experiment 4: PETN in Lucite Cylinder, Ytterbium Gage

The experimental layout is shown in Figure A-3. Two ytterbium stress gages were placed between the explosive and the inside wall of the lucite cylinder (Ex 1, Ex 2 in Figure A-3). The gages were placed near the midlength of the cylinder, one above the other and about 2.54 cm a part. Two additional ytterbium gages (Lu 1 and Lu 2 in Figure A-3) were placed 0.32 cm from the borehole periphery at the same level as the two gages at the explosive-lucite interface. A block of lucite was then glued over these two gages. The explosive source was again PETN pressed into a soda straw at a density of 0.6 g/cm^3.

The voltage records are shown in Figure A-4(a). These data were digitized and corrected for the gage response, and are given in Table A-1 and Figure A-5. The peak pressure and pulse

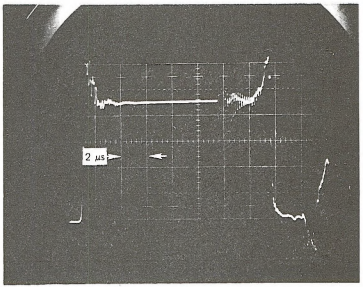

(a) EXPERIMENT 1 – PETN IN A STEEL PIPE

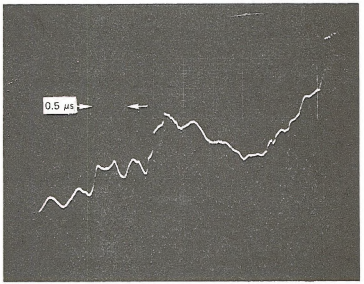

(b) EXPERIMENT 3 – PETN IN A LUCITE CYLINDER

MP-6700-18

FIGURE A-2 VOLTAGE RECORDS FROM EXPERIMENTS 1 AND 3

Table A-1

PEAK RADIAL COMPRESSIVE STRESSES AND PULSE DURATION IN BOREHOLE STRESS GAGE EXPERIMENTS

Experiment Number	Experimental Arrangement	Gage	Stress (GPa)	Duration (μs)
1	PETN at a density of 0.6 g/cm^3 in 4-mm-thick steel pipe	Manganin	1.5 (estimated)	1 to 3
2	PETN at a density of 0.6 g/cm^3 in a 5.1-cm-dia Lucite cylinder	Manganin	No data	No data
3	PETN at a density of 0.6 g/cm^3 in a 5.1-cm-dia Lucite cylinder	Manganin	1.5	1 to 3
4	PETN at a density of 0.6 g/cm^3 in a 5.1-cm-dia Lucite cylinder	Ex 1 Ytterbium	1.15	2 to 3
		Ex 2 Ytterbium	No data	No data
		Lu 1 Ytterbium	0.55	2 to 3
		Lu 2 Ytterbium	0.45	2 to 3
5	1.8-mm lead-sheathed MDF (5 grains PETN/ft) centered in a 7.5-mm-dia borehole in a 5.1-cm-dia Lucite cylinder	Ex 1 Ytterbium	0.60	2 to 3
		Ex 2 Ytterbium	0.58	2 to 3
		Lu 1 Ytterbium	No data	No data
		Lu 2 Ytterbium	0.23	2 to 3

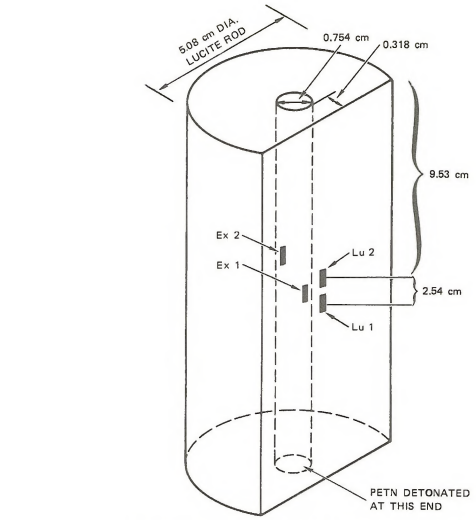

(a) CONFIGURATION OF EXPERIMENTS 4 AND 5; YTTERBIUM STRESS GAGES AT BOREHOLE BOUNDARY Ex 1, Ex 2 AND IN LUCITE ROD Lu 1, Lu 2

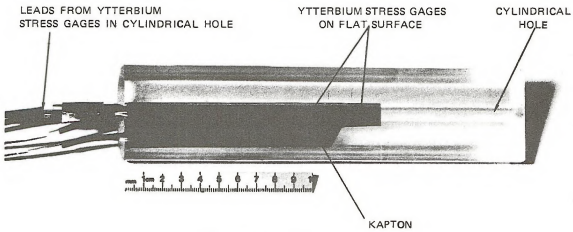

(b) INSTRUMENTED CYLINDRICAL LUCITE BLOCK

MP-6700-7A

FIGURE A-3 EXPERIMENTAL CONFIGURATION TO DETERMINE CHARACTERISTICS OF PETN AND MDF EXPLOSIVE SOURCES

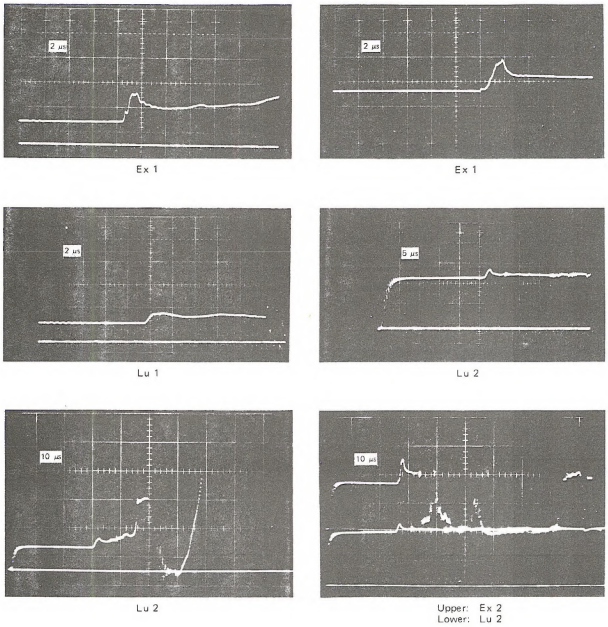

FIGURE A-4 VOLTAGE RECORDS FROM YTTERBIUM STRESS GAGES IN EXPERIMENTS 4 AND 5
No data from Ex 2 in Experiment 4 or from Lu 1 in Experiment 5 (see Figure A-3).

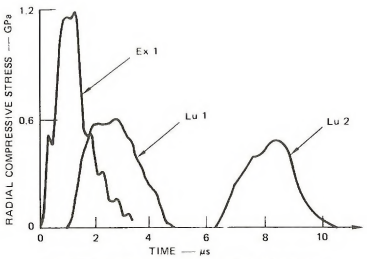

(a) EXPERIMENT 4 – PETN IN LUCITE CYLINDER

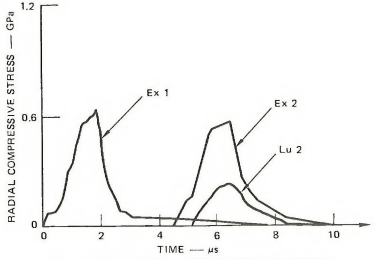

(b) EXPERIMENT 5 – MDF IN LUCITE CYLINDER

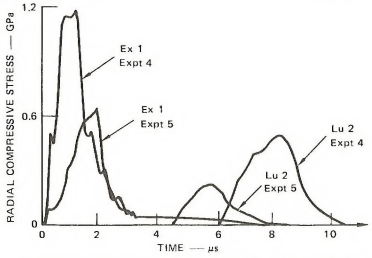

(c) COMPARISON OF RADIAL COMPRESSIVE STRESS HISTORIES FROM EXPERIMENTS 4 AND 5

MA-6700-20

FIGURE A-5 RADIAL COMPRESSIVE STRESS HISTORIES FROM EXPERIMENTS 4 AND 5

duration recorded at the explosive-solid interface were 1.2 GPa and 2 to 3 μs. The peak pressure and pulse duration recorded at 0.32 cm in the lucite was 0.6 GPa and 2 to 3 μs.

Experiment 5: MDF in Lucite Cylinder, Ytterbium Gage

The last experiment in this series used 1.8 mm (0.070 in.) diameter, lead-sheathed MDF (5 grains PETN/foot) in a soda straw as the explosive source. The MDF was centered in the straw using plastic spacers. The gage configuration and experimental setup were the same as in Experiment 4.

The voltage records are shown in Figure A-4(b). These data were digitized and corrected for the gage response; they are shown in Table A-1 and Figure A-5. The peak pressure and pulse duration at the borehole boundary are 0.6 GPa and 2 to 3 μs, respectively.

Parts of the lucite cylinder were recovered in this experiment and are shown in Figure A-6. The cracks in the lucite are elliptical (penny-shaped), elongate parallel to the cylinder axis, and are perpendicular to the borehole axis. These observations of cracks in the lucite verify that the tensile cracks modeled by the NAG-FRAG computational subroutine may be treated as penny-shaped cracks.

C. Conclusions

These borehole stress gage experiments demonstrated that:

- A borehole stress gage can be constructed successfully.
- The gage will survive a few microseconds after detonation of the explosive.
- The gage will return useful information about the radial compressive stress pulse shape of explosives at the borehole-shale boundary.

The experiments also provided information about the pulse shape of PETN and MDF, which helped guide the planning and construction of the springing experiments.

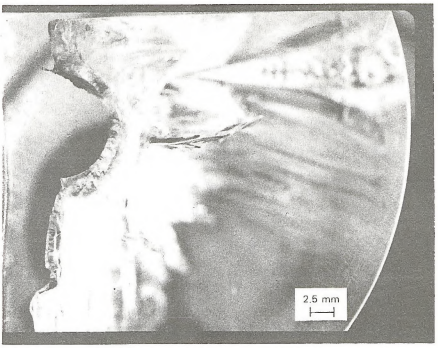

(a) END VIEW (Note that cracks are planar and extend parallel to the cylinder axis)

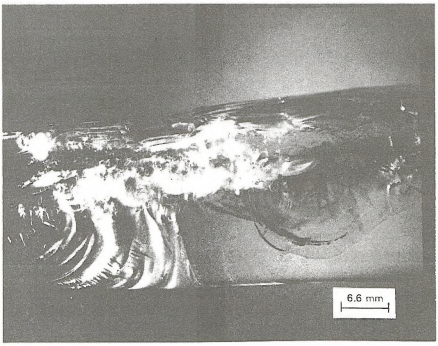

(b) SIDE VIEW (Note elliptical cracks)

MP-6700-21

FIGURE A-6 CRACKS IN LUCITE ROD PRODUCED BY MDF (5 GRAINS PETN/FOOT) IN EXPERIMENT 5

REFERENCES

1. D. A. Shockey, D. R. Curran, L. Seaman, J. T. Rosenberg, and C. F. Petersen, "Fragmentation of Rock Under Dynamic Loads," Int. J. Rock Mech. Sci. **11**, 303-317 (1974).

2. D. A. Shockey, D. R. Curran, M. Austin, and L. Seaman, "Development of a Capability for Predicting Cratering and Fragmentation Behavior in Rock," SRI Final Report to Defense Nuclear Agency, DNA 3730F (May 1975).

3. W. J. Murri, D. A. Shockey, and C. Young, "Dynamic Fracture and Fragmentation of Oil Shale," SRI Final Report to Los Alamos Scientific Laboratories, Los Alamos, New Mexico, SRI Project PYD-5650 (February 1977).

4. W. J. Murri, C. Young, D. A. Shockey, R. E. Tokheim and D. R. Curran, "Determination of Dynamic Fracture Parameters for Oil Shale," SRI Final Report to Sandia Laboratories, Albuquerque, New Mexico, SRI Project PYD-4046 (February 1977).

5. S. L. McHugh, L. Seaman, W. J. Murri, R. E. Tokheim and D. R. Curran, "Fracture and Fragmentation of Oil Shale," SRI Final Report to Sandia Laboratories, Albuquerque, New Mexico, SRI Project PYD-6128 (December 1977).

6. L. Seaman and D. A. Shockey, "Models for Ductile and Brittle Fracture for Two-Dimensional Wave Propagation Calculations," SRI Report to Army Materials and Mechanics Research Center, Watertown, Massachusetts, Report no. AMMRC CTR 75-2 (1975).

7. L. Seaman, D. R. Curran, and R. C. Crewdson, "Transformation of Observed Crack Traces on a Section to True Crack Density for Fracture Calculations," Appl. Physics **49**, 5221-5229 (October 1978).

8. D. A. Shockey, C. F. Petersen, D. R. Curran, and J. T. Rosenberg, "Failure of Rock Under High Rate Tensile Loads," *New Horizons in Rock Mechanics, Proc. 14th Symp. on Rock Mechanics*, p. 709-738, Pennsylvania State University, University Park, Pennsylvania (1972).

9. I. N. Sneddon, "The Distribution of Stress in the Neighborhood of a Crack in an Elastic Solid," Proc. Roy. Soc., A187, London (1946).

10. D. R. Curran, L. Seaman, and D. A. Shockey, "Dynamic Failure in Solids," Physics Today **30**, 46-55 (January 1977).

11. L. Seaman, D. R. Curran, and D. A. Shockey, "Computational Models for Ductile and Brittle Fracture," J. Appl. Physics **47** (11), 4814-4826 (1976).

12. B. W. Olinger, "Eastern Gas Shales Under Dynamic Stress," Report by Los Alamos Scientific Laboratory, Los Alamos, New Mexico, Report no. LA-UR-77-1937 (1977).

13. L. Seaman, "SRI PUFF 8 Computer Program for One-Dimensional Stress Wave Propagation," SRI Final Report, Part II, to U. S. Army Ballistic Research Laboratories, Aberdeen, Maryland, SRI Project PYU-6802 (August 1978).

14. H. C. Hornig, E. L. Lee, M. Finger, and J. E. Kurrie, "Equation of State of Detonation Products," *Proceedings Fifth Symposium (International) on Detonation ACR-184*, p. 503-512, Office of Naval Research, Department of the Navy, Arlington, Virginia (1970).

15. E. L. Lee and H. C. Hornig, "Equation of State of Detonation Product Gases," *Twelfth Symposium (International) on Combustion*, p. 493-499, The Combustion Institute, Pittsburgh, Pennsylvania (1969).

16. D. D. Keough, "Procedure for Fabrication and Operation of Manganin Shock Pressure Gages," SRI Technical Report to Air Force Weapons Laboratory, Report no. ARWL-TR-68-57 (August 1968).

17. M. J. Ginsberg, "Calibration and Characterizations of Ytterbium Stress Transducers," SRI Final Report to Defense Nuclear Agency, Report no. DNA 2742F (1971).

☆ U.S. GOVERNMENT PRINTING OFFICE: 1983-646-069/680